Pseudopotential lattice Boltzmann model with tunable coexistence densities and no interfacial velocity slip

Junren Hou [1], Shunli Jiang [1,2], Yugao Ma [3] and Shanfang Huang [1,*]

[1]*Department of Engineering Physics, Tsinghua University, Beijing 100084, China*

[2]*State Key Laboratory of Advanced Nuclear Energy Technology, Nuclear Power Institute of China, Chengdu 610213, China*

[3]*Nuclear Power Institute of China, Chengdu 610213, China*

(Received 18 February 2025; revised 12 June 2025; accepted 7 August 2025; published 28 August 2025)

The pseudopotential model in lattice Boltzmann method is widely used to simulate two-phase flows. Thermodynamic consistency is an important issue in the pseudopotential model. To achieve thermodynamic consistency, various force schemes have been proposed for the pseudopotential model. However, their performance under transient and moving conditions remains insufficiently validated. We evaluate existing force schemes and find that most of them suffer from interfacial velocity slip. A Chapman-Enskog analysis reveals that these schemes introduce error terms in the macroscopic equations, leading to the interfacial velocity slip. While other schemes avoid this slip, they fail to achieve thermodynamic consistency. To address this issue, we propose a novel pseudopotential model achieving thermodynamic consistency while preventing interfacial velocity slip. Our model introduces a new pseudopotential force by adding a term $2\gamma\nabla^2\psi\nabla\psi + O(\nabla^5)$ to the original force. Here, ψ represents the pseudopotential and the coefficient γ is used to tune the coexistence densities. The applicability of our model under moving conditions is validated through simulations of two-phase Couette flow and two-phase Poiseuille flow. Numerical results confirm that our model achieves second-order accuracy. The transient results of our model are compared with those of volume of fluid method, validating the applicability of our model under transient conditions. Finally, droplet splashing and liquid film evaporation under shear flow are also simulated to demonstrate our model's capability for simulating two-dimensional flow and interphase mass transfer.

DOI: 10.1103/kpjp-fynh

I. INTRODUCTION

Multiphase flow is a prevalent physical phenomenon in nature and plays a critical role in various fields, including microelectronics [1], nuclear energy [2] and the chemical industry [3]. Numerical simulations have become an essential tool for studying multiphase flow, particularly in scenarios where experimental approaches are infeasible [3–5]. Among the methods commonly used to simulate multiphase flow, the volume of fluid (VOF) method [6] and the level set method [7] are two widely adopted macroscopic approaches. Despite their popularity, both methods face challenges, particularly in modeling porous media and accurately capturing wall contact angles. The lattice Boltzmann method (LBM), a mesoscopic approach [8], has shown great potential for simulating multiphase flow. Common multiphase lattice Boltzmann (LB) models include the free-energy model [9], the color-gradient model [10], the pseudopotential model [11,12], and the phase-field model [13,14]. Among these, the pseudopotential model has attracted significant attention due to its conceptual simplicity, computational efficiency and kinetic properties [15].

The pseudopotential model was first proposed by Shan and Chen in 1993 [11]. In this model, a simple pseudopotential force is incorporated into the standard LB framework to represent intermolecular forces. By including this pseudopotential force, the model can effectively capture phase transitions and phase separation without requiring explicit tracking of the liquid-gas interface. This feature quickly gained significant attention within the scientific community. Building on Shan and Chen's foundational work [11,12], He and Doolen [16] extended the pseudopotential model to accommodate a wide range of equations of state (EOS). Yuan and Laura [17] further explored various EOS formulations and provided guidelines for their selection. Recently, the EOS in Helmholtz energy form is also introduced to the pseudopotential model by Zheng and Huang [18]. At the same time, numerous applications of the pseudopotential model have been studied. For instance, Chen *et al.* [4] conducted LB simulations of microchannel flow boiling to enhance heat dissipation, while Gong *et al.* [19,20] applied the model to investigate nanoscale evaporation heat transfer. Recently, Hou *et al.* [21] extended the pseudopotential model to the field of supercritical fluid thermal convection.

As highlighted in the previous paragraph, the pseudopotential force is fundamental to the pseudopotential model, and various force schemes have been developed to incorporate it. Shan and Chen initially introduced a force scheme [11], but the liquid-gas coexistence densities in this scheme were found to vary with viscosity [22]. Guo *et al.* [23] proposed an alternative force scheme in which the coexistence densities are independent of viscosity. McCracken and Abraham [24] further developed a multiple-relaxation-time (MRT) force scheme for multiphase flow, which was later identified

*Contact author: sfhuang@mail.tsinghua.edu.cn

as the MRT version of Guo *et al.*'s scheme [15]. To achieve large density ratios, Kupershtokh *et al.* [25] proposed the exact difference method (EDM) scheme.

Despite these advancements, all above schemes suffer from thermodynamic inconsistency. In a liquid-gas equilibrium system, the coexistence densities are expected to be determined by the Maxwell area construction. However, the coexistence densities predicted by the pseudopotential model often deviate from those given by the Maxwell construction, a phenomenon known as thermodynamic inconsistency. Shan and Chen [9] demonstrated that thermodynamic consistency can only be achieved if the pseudopotential is defined as $\psi = \psi_0 \exp(-\rho_0/\rho)$, where ρ is the density, ψ is the pseudopotential and ρ_0 and ψ_0 are adjustable parameters. Under this definition, however, the EOS is fixed to a specific form and cannot be freely adjusted.

To achieve thermodynamic consistency, various improved force schemes have been proposed for the pseudopotential model. Li *et al.* [26] compared the Shan-Chen, EDM and Guo *et al.*'s force schemes. They found that both the Shan-Chen and EDM schemes introduce a similar additional term in the macroscopic equations, which enhances their stability compared to Guo *et al.*'s scheme. Based on their analysis, Li *et al.* proposed an improved scheme that incorporates this additional term, achieving thermodynamic consistency by tuning the coexistence densities. Subsequently, they [27] further developed the corresponding MRT version of their force scheme. Lycett-Brown and Luo [28] conducted a third-order Chapman-Enskog (CE) analysis of a general forcing term and found that the EDM scheme introduces a high-order error term. Similar to Li *et al.* [26,27], they developed a force scheme capable of adjusting the coexistence densities. Additionally, they observed that increasing the interface thickness reduces the error in gas density. Huang and Wu [29] performed a third-order CE analysis of the McCracken-Abraham scheme and identified a third-order isotropic term in the scheme. Based on their analysis, they proposed an improved scheme that allows for the adjustment of coexistence densities. Zheng *et al.* [30] also conducted a third-order CE analysis on various force schemes, including the Shan-Chen, EDM and Guo *et al.*'s schemes. Building on Li *et al.*'s work [26,27], they proposed an improved scheme that facilitates the adjustment of coexistence densities. Recently, Huang *et al.* [31–33] developed a lattice Boltzmann model with a self-tuning equation of state (ST-EOS model). This model combines the advantages of the pseudopotential model and the free-energy model, inherently satisfying thermodynamic consistency. Third-order CE analysis was also employed in their work. Additionally, Li *et al.* [34] compared five commonly used EOS within the ST-EOS model. Their findings indicated that the maximum density ratios achieved by different EOS are comparable and that increasing the interface thickness leads to higher density ratios.

From the above discussion, it is evident that the interface thickness is closely related to coexistence densities. In the LB community, modifying the EOS is a widely used method for adjusting the interface thickness. Wagner and Pooley [35] were among the first to investigate the effect of EOS on interface thickness. They introduced a scaling factor k into the EOS and found that decreasing k increases the interface thickness, which, in turn, results in a larger liquid-gas density ratio. This approach has since been widely adopted in the pseudopotential community [36,37]. Notably, both Lycett-Brown *et al.*'s scheme [28] and the ST-EOS model [31] utilize this method to adjust the interface thickness. Additionally, adjusting the coefficient in the EOS has also been shown to influence the interface thickness. For example, Li *et al.* [27] demonstrated that the interface thickness is approximately proportional to $1/\sqrt{a}$, where a is a coefficient in the Carnahan-Starling EOS.

Although significant progress has been made in the development of pseudopotential models, several research gaps remain. As highlighted in the literature review, high-order CE analysis is widely employed in the development of force schemes. To simplify the analysis, steady-state and stationary assumptions are commonly adopted in performing higher-order CE expansions of force schemes [28–31,38]. However, the applicability of these proposed force schemes under transient and moving conditions has not been adequately validated. Furthermore, while modifying the EOS to adjust the interface thickness is a common method, the physical meaning of this adjustment remains unclear.

In this paper, we assess the applicability of various popular force schemes under moving conditions. Our findings reveal that most of these schemes suffer from interfacial velocity slip. To address this issue, we propose a novel pseudopotential model with tunable coexistence densities and no interfacial velocity slip. Additionally, we provide a comprehensive discussion on the underlying mechanisms of adjusting the interface thickness by modifying the EOS.

The rest of the paper is organized as follows. Section II introduces the Maxwell construction and discusses the mechanical stability of the pseudopotential model. Section III summarizes existing popular force schemes and verifies our codes by comparing liquid-gas coexistence densities. Interfacial velocity slip is discussed in Sec. IV. Section V introduces our new pseudopotential force model, which is validated under moving and transient conditions in Sec. VI. Finally, the main findings of this study are summarized in Sec. VII.

II. THERMODYNAMIC INCONSISTENCY

Thermodynamic inconsistency is a primary concern in the pseudopotential community. In this section, we provide a detailed discussion of this issue.

A. Macroscopic equations and Maxwell construction

For a two-phase system described by a given EOS, the mass and momentum transport equations are as follows [16,33]:

$$\frac{\partial \rho}{\partial t} + \nabla \cdot (\rho \boldsymbol{u}) = 0, \tag{1a}$$

$$\frac{\partial (\rho \boldsymbol{u})}{\partial t} + \nabla \cdot (\rho \boldsymbol{u}\boldsymbol{u}) = -\nabla \cdot \mathbf{P} + \nabla \cdot \mathbf{\Pi} + \boldsymbol{F}, \tag{1b}$$

where t is time, $\boldsymbol{u}$ is the velocity, and $\boldsymbol{F}$ represents the force. The pressure tensor $\mathbf{P}$ and the viscous stress tensor $\mathbf{\Pi}$ are

given by

$$\mathbf{\Pi} = \mu(\nabla \boldsymbol{u} + \nabla \boldsymbol{u}^{\mathrm{T}}) + \left(\xi - \frac{2}{D}\mu\right)\nabla \cdot \boldsymbol{u}, \tag{2a}$$

$$\mathbf{P} = \left(p_{\mathrm{EOS}} - \frac{\kappa}{2}\nabla\rho \cdot \nabla\rho - \kappa\rho\nabla^2\rho\right)\mathbf{I} + \kappa\nabla\rho\nabla\rho, \tag{2b}$$

where μ is the dynamic viscosity, ξ is the bulk viscosity, p_{EOS} is the pressure given by the EOS, D is the number of spatial dimensions, and $\mathbf{I}$ represents the identity matrix. The parameter κ is related to the surface tension.

Next, we consider a steady, stationary, and one-dimensional problem where the liquid-gas interface is parallel to the y-z plane. In this case, the normal pressure P_{n} can be expressed as

$$P_{\mathrm{n}} = P_{xx} = p_{\mathrm{EOS}} - \kappa\rho\frac{\mathrm{d}^2\rho}{\mathrm{d}x^2} + \frac{\kappa}{2}\left(\frac{\mathrm{d}\rho}{\mathrm{d}x}\right)^2. \tag{3}$$

From Eq. (3), we obtain

$$\frac{2}{\kappa}[p_{\mathrm{EOS}}(\rho) - P_{\mathrm{n}}]\frac{1}{\rho^2} = \frac{\mathrm{d}}{\mathrm{d}\rho}\left[\frac{1}{\rho}\left(\frac{\mathrm{d}\rho}{\mathrm{d}x}\right)^2\right]. \tag{4}$$

Since $\mathrm{d}\rho/\mathrm{d}x = 0$ in the single-phase region, integrating Eq. (4) from the gas density ρ_{gas} to the liquid density ρ_{liq}, we obtain

$$\int_{\rho_{\mathrm{gas}}}^{\rho_{\mathrm{liq}}} [p_{\mathrm{EOS}}(\rho) - P_{\mathrm{n}}]\frac{1}{\rho^2}\,\mathrm{d}\rho = 0, \tag{5}$$

where $\upsilon = 1/\rho$ denotes the specific volume. Equation (5) corresponds to the Maxwell area construction [39].

B. Pseudopotential force and its mechanical stability

The pseudopotential force proposed by Shan and Chen [11,12] is expressed as

$$\boldsymbol{F}_{\mathbf{pp}} = -G\psi(\boldsymbol{x}, t)\sum_i w(|\boldsymbol{e_i}/c|^2)\psi(\boldsymbol{x} + \boldsymbol{e_i}\delta_t, t)\boldsymbol{e_i}, \tag{6}$$

where G is a parameter controlling the strength of the pseudopotential force, $\boldsymbol{x}$ is the position vector and δ_t is the time step. Additionally, $c = \delta_x/\delta_t$ is the lattice speed, where δ_x represents the spatial step. The weights are defined as $w(1) = 1/3$ and $w(2) = 1/12$. Without loss of generality, the D2Q9 discrete velocity set [40] is employed.

Next, a Taylor expansion of Eq. (6) at $\boldsymbol{x}$, neglecting higher-order terms of $O(\nabla^5)$, yields

$$\begin{aligned}\boldsymbol{F}_{\mathbf{pp}} &= -Gc\delta_x\psi\nabla\psi - \kappa_{\mathrm{pp}}\psi\nabla\nabla\cdot\nabla\psi \\ &= -\frac{Gc\delta_x}{2}\nabla\cdot(\psi^2\mathbf{I}) - \kappa_{\mathrm{pp}}\nabla\cdot[a_1\nabla\psi\nabla\psi \\ &\quad + a_2\psi\nabla\nabla\psi + (a_3\nabla\psi\cdot\nabla\psi + a_4\psi\nabla\cdot\nabla\psi)\mathbf{I}],\end{aligned} \tag{7}$$

where $\kappa_{\mathrm{pp}} = Gc\delta_x^3/6$ and the free parameters a_{1-4} satisfy the following relations [29]:

$$a_1 + a_2 + 2a_3 = 0, \quad a_1 + a_4 = 0, \quad a_2 + a_4 = 1. \tag{8}$$

From Eq. (1b), it is evident that the roles of $\boldsymbol{F}$ and $\nabla\cdot\mathbf{P}$ are analogous. The pseudopotential force can thus be interpreted as a contribution to the pressure tensor, i.e., $\boldsymbol{F}_{\mathbf{pp}} = -\nabla\cdot\boldsymbol{P}_{\mathbf{pp}}$. The corresponding pressure tensor is expressed as

$$\begin{aligned}\mathbf{P}_{\mathbf{pp}} &= \frac{Gc\delta_x}{2}\psi^2\mathbf{I} + \kappa_{\mathrm{pp}}[(a_3\nabla\psi\cdot\nabla\psi + a_4\psi\nabla^2\psi)\mathbf{I} \\ &\quad + a_1\nabla\psi\nabla\psi + a_2\psi\nabla\nabla\psi].\end{aligned} \tag{9}$$

At this point, the total pressure tensor is given as $\mathbf{P} = p_{\mathrm{LBE}}\mathbf{I} + \mathbf{P}_{\mathbf{pp}}$, where $p_{\mathrm{LBE}} = \rho c_s^2$ is the pressure from the LB equation and $c_s = c/\sqrt{3}$ is the sound speed [40]. By comparing Eq. (2) with Eq. (9), it follows that the pseudopotential ψ must satisfy the following form to accommodate arbitrary EOS:

$$\psi = \sqrt{\frac{2(p_{\mathrm{EOS}} - p_{\mathrm{LBE}})}{Gc\delta_x}}. \tag{10}$$

In this formulation, G does not influence the results and $G = -1$ is chosen to ensure that the expression under the square root is positive. For a steady, stationary and one-dimensional problem, the normal pressure is expressed as

$$P_{\mathrm{n}} = p_{\mathrm{EOS}} + \frac{\kappa_{\mathrm{pp}}}{2}\left[A\left(\frac{\mathrm{d}\psi}{\mathrm{d}x}\right)^2 + B\psi\frac{\mathrm{d}^2\psi}{\mathrm{d}x^2}\right], \tag{11}$$

where $A = -1$ and $B = 2$. Referring to Appendix A in Ref. [27], Eq. (11) can be rewritten as

$$(P_{\mathrm{n}} - p_{\mathrm{EOS}})\frac{\psi'}{\psi^{1+\epsilon}} = \frac{\kappa_{\mathrm{pp}}}{2}\frac{\mathrm{d}}{\mathrm{d}\rho}\left[\frac{(\psi')^2}{\psi^{\epsilon}}\left(\frac{\mathrm{d}\rho}{\mathrm{d}x}\right)^2\right], \tag{12}$$

where $\psi' = \mathrm{d}\psi/\mathrm{d}\rho$ and $\epsilon = -2A/B = 1$. Integrating Eq. (12) from ρ_{gas} to ρ_{liq}, the mechanical stability condition is obtained as

$$\int_{\rho_{\mathrm{gas}}}^{\rho_{\mathrm{liq}}} (p_{\mathrm{EOS}} - P_{\mathrm{n}})\frac{\psi'}{\psi^{1+\epsilon}}\,\mathrm{d}\rho = 0. \tag{13}$$

Comparing Eq. (5) with Eq. (13), it is evident that the mechanical stability condition deviates from the Maxwell area construction, leading to thermodynamic inconsistency in the pseudopotential model. This inconsistency is reflected in the coexistence densities predicted by the pseudopotential model, which fail to satisfy the thermodynamic equilibrium dictated by the Maxwell construction. Notably, Eq. (13) contains a coefficient ϵ, which can be tuned to achieve results consistent with the Maxwell construction. This approach has been widely adopted in the pseudopotential community [26–29]. It is important to state that thermodynamic consistency is not only just consistency in the coexistence densities between the LBM results and the Maxwell construction, but also includes other aspects such as chemical potential consistency [9]. In this paper, we will only discuss the coexistence densities consistency, which is the focus of attention in the pseudopotential community.

III. EXISTING FORCE SCHEMES

A. Introduction and comparison of various force schemes

Existing force schemes can be broadly classified into two categories: single-relaxation-time (SRT) schemes and multiple-relaxation-time (MRT) schemes. The SRT schemes can be expressed in the following unified form:

Collision:

$$f_i^*(\boldsymbol{x},t) = -\frac{1}{\tau}\left[f_i(\boldsymbol{x},t) - f_i^{\mathrm{eq}}(\boldsymbol{x},t)\right] + F_i. \tag{14}$$

Streaming:

$$f_i(\boldsymbol{x}+\boldsymbol{e_i}\delta_t, t+\delta_t) - f_i(\boldsymbol{x},t) = f_i^*(\boldsymbol{x},t). \tag{15}$$

Macroscopic values:

$$\rho = \sum_i f_i, \quad \rho\boldsymbol{u} = \sum_i \boldsymbol{e_i} f_i + \frac{\delta_t}{2}\boldsymbol{F}. \tag{16}$$

Equilibrium density distribution function:

$$f_i^{\mathrm{eq}} = \rho\omega_i\left[1 + \frac{\boldsymbol{e_i}\cdot\boldsymbol{u}^{\mathbf{eq}}}{c_s^2} + \frac{(\boldsymbol{e_i}\cdot\boldsymbol{u}^{\mathbf{eq}})^2}{2c_s^4} - \frac{(\boldsymbol{u}^{\mathbf{eq}})^2}{2c_s^2}\right]. \tag{17}$$

Here, f_i represents the density distribution function, F_i denotes the force contribution to the distribution function and $\tau = \nu/(c_s^2\delta_t) + 0.5$ is the dimensionless relaxation time, where ν is the kinematic viscosity. $\boldsymbol{u}^{\mathbf{eq}}$ is the equilibrium velocity used to compute f_i^{eq} and ω_i are the weights defined as $\omega_0 = 4/9$, $\omega_{1-4} = 1/9$ and $\omega_{5-8} = 1/36$ for the D2Q9 discrete velocity set [40]. The total force $\boldsymbol{F}$ consists of two components: $\boldsymbol{F} = \boldsymbol{F}_{\mathbf{pp}} + \boldsymbol{F}_{\mathbf{ext}}$, where $\boldsymbol{F}_{\mathbf{pp}}$ is the pseudopotential force and $\boldsymbol{F}_{\mathbf{ext}}$ is the external force. The common SRT schemes are summarized as follows:

(1) *SRT: Shan-Chen Scheme* [11]

$$F_i = 0, \quad \rho\boldsymbol{u}^{\mathbf{eq}} = \sum_i \boldsymbol{e_i} f_i + \tau\delta_t\boldsymbol{F}. \tag{18}$$

(2) *SRT: Guo et al.'s Scheme* [23]

$$F_i = \delta_t\omega_i\left(1 - \frac{1}{2\tau}\right)\left[\frac{\boldsymbol{e_i}-\boldsymbol{u}}{c_s^2} + \frac{(\boldsymbol{e_i}\cdot\boldsymbol{u})\boldsymbol{e_i}}{c_s^4}\right]\cdot\boldsymbol{F}, \tag{19a}$$

$$\boldsymbol{u}^{\mathbf{eq}} = \boldsymbol{u}. \tag{19b}$$

(3) *SRT: EDM Scheme* [25]

$$F_i = f_i^{\mathrm{eq}}(\rho, \boldsymbol{u}^* + \Delta\boldsymbol{u}) - f_i^{\mathrm{eq}}(\rho,\boldsymbol{u}^*), \quad \boldsymbol{u}^{\mathbf{eq}} = \boldsymbol{u}, \tag{20}$$

where $\rho\boldsymbol{u}^* = \sum_i \boldsymbol{e_i} f_i$ and $\Delta\boldsymbol{u} = \delta_t\boldsymbol{F}/\rho$.

(4) *SRT: Li et al.'s Scheme* [26]

$$F_i = \delta_t\omega_i\left(1 - \frac{1}{2\tau}\right)\left[\frac{\boldsymbol{e_i}-\boldsymbol{v}}{c_s^2} + \frac{(\boldsymbol{e_i}\cdot\boldsymbol{v})\boldsymbol{e_i}}{c_s^4}\right]\cdot\boldsymbol{F}, \tag{21a}$$

$$\boldsymbol{u}^{\mathbf{eq}} = \boldsymbol{u}, \tag{21b}$$

where $\boldsymbol{v} = \boldsymbol{u} + \sigma\boldsymbol{F}_{\mathbf{pp}}/[(\tau-0.5)\psi^2]$. Here, σ is a coefficient used to adjust the coexistence densities.

Due to their enhanced stability, MRT force schemes are generally preferred over SRT schemes. The streaming step and macroscopic value calculations in the MRT model are consistent with those in the SRT model [see Eqs. (15) and (16)]. The core concept of the MRT scheme is to perform the collision step in momentum space [41]. The density distribution function is transformed into momentum space through matrix operations, given by $\mathbf{m} = \mathbf{M}\mathbf{f}$, where $\mathbf{f} = [f_0, f_1, f_2, \ldots, f_8]^{\mathrm{T}}$ and $\mathbf{m} = [m_0, m_1, m_2, \ldots, m_8]^{\mathrm{T}}$. The dimensionless orthogonal transformation matrix $\mathbf{M}$ is chosen as

$$\mathbf{M} = \begin{pmatrix} 1 & 1 & 1 & 1 & 1 & 1 & 1 & 1 & 1 \\ -4 & -1 & -1 & -1 & -1 & 2 & 2 & 2 & 2 \\ 4 & -2 & -2 & -2 & -2 & 1 & 1 & 1 & 1 \\ 0 & 1 & 0 & -1 & 0 & 1 & -1 & -1 & 1 \\ 0 & -2 & 0 & 2 & 0 & 1 & -1 & -1 & 1 \\ 0 & 0 & 1 & 0 & -1 & 1 & 1 & -1 & -1 \\ 0 & 0 & -2 & 0 & 2 & 1 & 1 & -1 & -1 \\ 0 & 1 & -1 & 1 & -1 & 0 & 0 & 0 & 0 \\ 0 & 0 & 0 & 0 & 0 & 1 & -1 & 1 & -1 \end{pmatrix}. \tag{22}$$

In contrast to the SRT model, the collision step in the MRT model is expressed as

$$\mathbf{m}^* = -\mathbf{\Lambda}(\mathbf{m} - \mathbf{m}^{\mathbf{eq}}) + \delta_t\left(\mathbf{I} - \frac{\mathbf{\Lambda}}{2}\right)\mathbf{F}_{\mathbf{m}}, \tag{23}$$

where the diagonal relaxation matrix $\mathbf{\Lambda}$ is defined as

$$\mathbf{\Lambda} = \mathrm{diag}\left[\frac{1}{\tau_{\mathrm{c}}}, \frac{1}{\tau_\xi}, \frac{1}{\tau_e}, \frac{1}{\tau_{\mathrm{c}}}, \frac{1}{\tau_q}, \frac{1}{\tau_{\mathrm{c}}}, \frac{1}{\tau_q}, \frac{1}{\tau_\nu}, \frac{1}{\tau_\nu}\right]. \tag{24}$$

Here, τ_{c} corresponds to conserved quantities, while τ_e and τ_q are tunable coefficients that impact model stability. τ_ν and τ_ξ are associated with viscosity and are defined as

$$\tau_\nu = \frac{\nu}{c_s^2\delta_t} + 0.5, \quad \tau_\xi = \frac{\xi}{\rho c_s^2\delta_t} + 0.5. \tag{25}$$

In this study, all coefficients in Eq. (24) except τ_ν are set to 1. The density distribution function is transformed back into velocity space for the streaming step using $\mathbf{f}^* = \mathbf{M}^{-1}\mathbf{m}^*$, where $\mathbf{M}^{-1}$ is the inverse matrix of $\mathbf{M}$. The equilibrium distribution function in momentum space is expressed as

$$\mathbf{m}^{\mathbf{eq}} = \rho\big(1, -2+3|\bar{\boldsymbol{u}}|^2, 1-3|\bar{\boldsymbol{u}}|^2, \bar{u}_x, -\bar{u}_x, \bar{u}_y, -\bar{u}_y, \bar{u}_x^2 - \bar{u}_y^2, \bar{u}_x\bar{u}_y\big)^{\mathrm{T}}. \tag{26}$$

Here, the overline $\bar{\cdot}$ (e.g., $\bar{u}_x, \bar{F}_x$) indicates variables normalized by the lattice speed c.

The common MRT schemes are summarized as follows:

(1) *MRT: McCracken-Abraham scheme* [24]

$$\mathbf{F}_{\mathbf{m}} = [0, 6\bar{\boldsymbol{F}}\cdot\bar{\boldsymbol{u}}, -6\bar{\boldsymbol{F}}\cdot\bar{\boldsymbol{u}}, \bar{F}_x, -\bar{F}_x, \bar{F}_y, -\bar{F}_y, 2(\bar{F}_x\bar{u}_x - \bar{F}_y\bar{u}_y), \bar{F}_x\bar{u}_y + \bar{F}_y\bar{u}_x]^{\mathrm{T}}. \tag{27}$$

(2) *MRT: Li et al.'s scheme* [27]

The first and second components of $\mathbf{F}_{\mathbf{m}}$ in Eq. (27) are modified as

$$F_{\mathrm{m1}} = 6\bar{\boldsymbol{F}}\cdot\bar{\boldsymbol{u}} + \frac{12\sigma|\bar{\boldsymbol{F}}_{\mathbf{pp}}|^2}{\psi^2\delta_t(\tau_\xi - 0.5)}, \tag{28a}$$

$$F_{\mathrm{m2}} = -6\bar{\boldsymbol{F}}\cdot\bar{\boldsymbol{u}} + \frac{12\sigma|\bar{\boldsymbol{F}}_{\mathbf{pp}}|^2}{\psi^2\delta_t(\tau_e - 0.5)}, \tag{28b}$$

where σ is a coeffcient used to adjust the coexistence densities.

TABLE I. Comparison of various force schemes. The second column lists the corresponding ϵ values of the force schemes. The third column indicates whether the force scheme achieves thermodynamic consistency, where ✓ denotes that thermodynamic consistency is achieved and ✗ denotes that it is not achieved. The fourth column indicates whether the force scheme suffers from interfacial velocity slip, where ✓ denotes that interfacial velocity slip is eliminated and ✗ denotes that it exists.

Force schemes	Parameter ϵ	Consistency	Velocity slip
SRT: Shan-Chen [11]	Unknown	✗	✗
SRT: Guo *et al.* [23]	0	✗	✓
SRT: EDM [25]	$\epsilon = -2Gc_s^2\psi^2/\rho$	✗	✗
SRT: Li *et al.* [26]	$\epsilon = -16G\sigma$	✓	✗
MRT: McCracken-Abraham [24]	0	✗	✓
MRT: Li *et al.* [27]	$\epsilon = -16G\sigma$	✓	✗
MRT: Huang-Wu [29]	$\epsilon = -8(k_1 + k_2)$	✓	✗
MRT: ST-EOS [31]	/	✓	✗

(3) *MRT: Huang-Wu scheme* [29]

This scheme introduces an additional term $\mathbf{\Lambda Q_m}$ into Eq. (23), where

$$\mathbf{Q_m} = \left[0, 3(k_1+2k_2)\frac{|\bar{\boldsymbol{F}}_{\mathbf{pp}}|^2}{G\psi^2}, -3(k_1+2k_2)\frac{|\bar{\boldsymbol{F}}_{\mathbf{pp}}|^2}{G\psi^2}, 0, 0, 0, 0, k_1\frac{\bar{F}_{\mathrm{pp},x}^2 - \bar{F}_{\mathrm{pp},y}^2}{G\psi^2}, k_1\frac{\bar{F}_{\mathrm{pp},x}\bar{F}_{\mathrm{pp},y}}{G\psi^2}\right]^{\mathrm{T}}, \tag{29}$$

where k_1 and k_2 are coeffcients used to adjust the coexistence densities.

(4) *MRT: ST-EOS scheme* [31]

This scheme inherently achieves thermodynamic consistency. Due to its complexity and differences from the above schemes, detailed descriptions are omitted here. We adopt the implementation described in Refs. [34,42]. Furthermore, the SR-EOS model is very different from the pseudopotential model. To some extent it cannot be grouped into the pseudopotential LB methods.

The corresponding values of ϵ for various force schemes are summarized in Table I. We have selected the eight force schemes mentioned above not only because they are widely used, but also because they are highly representative. That is, most other schemes either borrow ideas from these schemes or have been shown to be equivalent to them. For instance, Li *et al.* [15] has demonstrated that Wagner's scheme [43] is equivalent to Guo *et al.*'s scheme, while the schemes proposed by Lycett-Brown and Luo [28,44] are largely based on Li *et al.*'s scheme, with a modification to the F_i term of the Guo *et al.* scheme. Additionally, the decoupled and stabilized lattice Boltzmann method proposed by Wu *et al.* [45] also incorporates the $\mathbf{Q_m}$ term from the Huang-Wu scheme to ensure thermodynamic consistency. We believe that these eight schemes can represent all existing force schemes in the pseudopotential community.

B. Coexistence densities under stationary conditions

In this section, the coexistence densities for various schemes are presented to provide a detailed comparison of their performance. Additionally, these results serve to validate the accuracy of our codes. The EOS adopted in this work is the Peng-Robinson EOS [17], which is expressed as

$$p_{\mathrm{EOS}} = \frac{\rho RT}{1-b\rho} - \frac{a\varphi(T)\rho^2}{1+2b\rho-b^2\rho^2}, \tag{30}$$

where $\varphi(T) = [1 + (0.37464 + 1.54226\omega - 0.26992\omega^2)(1-\sqrt{T/T_c})]^2$, $a = 0.45724R^2T_c^2/p_c$, and $b = 0.0778RT_c/p_c$. Here, R represents the gas constant, ω is the acentric factor, T is the temperature, p is the pressure, and the subscript c denotes critical point properties. In this work, we use the values $a = 2/49$, $b = 2/21$, $R = 1$, and $\omega = 0.344$ [4,17]. Unless otherwise indicated, δ_x and δ_t are taken as 1 in this study.

To obtain the coexistence densities, a one-dimensional flat plate is simulated. The computational domain length L_x is set to 200 and the domain width L_y is set to 2, corresponding to a lattice size of $N_x \times N_y = 201 \times 3$. Periodic boundary conditions are applied. The convergence criterion is defined as

$$\max\left|\frac{\rho(\boldsymbol{x},t) - \rho(\boldsymbol{x},t-\delta_t)}{\rho(\boldsymbol{x},t-\delta_t)}\right| < 10^{-9}. \tag{31}$$

The density field is initialized as

$$\rho(\boldsymbol{x},0) = \frac{\rho_{\mathrm{liq}}+\rho_{\mathrm{gas}}}{2} - \frac{\rho_{\mathrm{liq}}-\rho_{\mathrm{gas}}}{2}\tanh\frac{2(|x-L_x/2|-L_x/4)}{W_{\mathrm{init}}}, \tag{32}$$

where the initial interface thickness W_{init} is set to 5. Here, ρ_{liq} and ρ_{gas} represent the liquid and gas densities, respectively, which are determined by the mechanical stability condition. For the Shan-Chen and EDM schemes, solving the mechanical stability condition is challenging, so the initial densities are instead determined using the Maxwell construction.

Figure 1(a) presents the coexistence densities for the Shan-Chen scheme, showing that the coexistence curve varies with ν. This phenomenon is consistent with the findings of Huang *et al.* [22]. Figure 1(b) illustrates that the coexistence densities of the EDM scheme are independent of viscosity. By comparing Figs. 1(a) and 1(b), it can be observed that the coexistence densities for the Shan-Chen and EDM schemes coincide when $\tau = 1$. This occurs because, under this condition, the dimensionless relaxation time τ equals 1, making the two schemes equivalent, as reported by Li *et al.* [26]. Figure 1(c) compares the coexistence densities of Guo *et al.*'s scheme and the McCracken-Abraham scheme. The results show good agreement with the mechanical stability condition for $\epsilon = 0$, confirming that the McCracken-Abraham scheme is the MRT version of Guo *et al.*'s scheme [15]. The McCracken-Abraham scheme is employed for the following computations in this

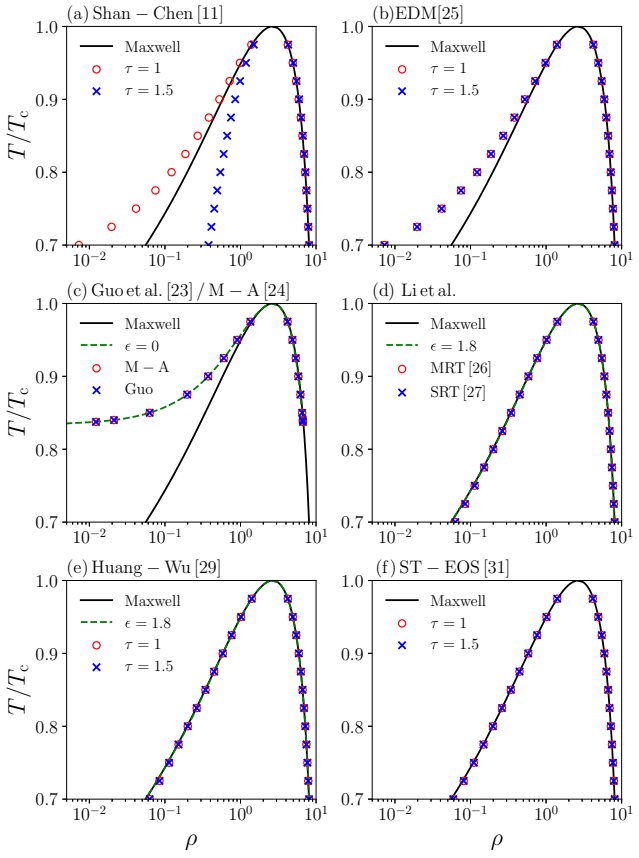

FIG. 1. Coexistence densities of existing schemes. Black solid lines represent the coexistence densities given by Maxwell construction. Green dashed lines represent the coexistence densities given by mechanical stability. The kinematic viscosity τ in panels (c) and (d) is 1.

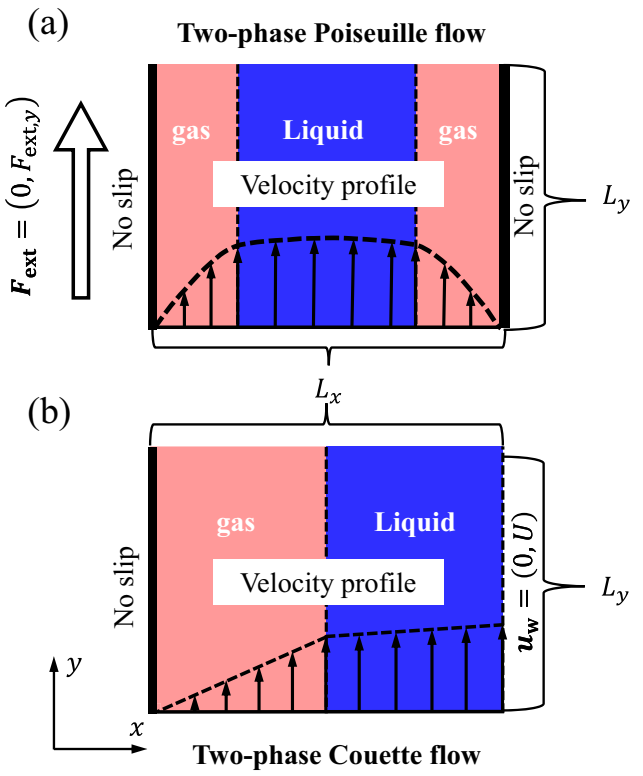

FIG. 2. Schematic diagrams of the two-phase (a) Poiseuille and (b) Couette flows.

study. Figures 1(d) and 1(e) display the coexistence densities for Li *et al.*'s scheme and the Huang-Wu scheme, respectively. In this paper, the parameter σ in Li *et al.*'s scheme is set to 0.1125, while the parameters k_1 and k_2 in the Huang-Wu scheme are set to -0.1125. The corresponding value of ϵ is 1.8. The results align well with the mechanical stability condition and the Maxwell construction, demonstrating that thermodynamic consistency can be achieved by tuning ϵ. The coexistence densities for the ST-EOS model are shown in Fig. 1(f). Following the settings of Li *et al.* [34], the interface thickness is fixed at 10 and the surface tension is set to 0.01. The results exhibit excellent agreement with the Maxwell construction, confirming that the ST-EOS model inherently satisfies thermodynamic consistency. In summary, the results in Fig. 1 are consistent with analytical solutions and previous studies, validating the accuracy of our codes. The performance of various schemes in terms of thermodynamic consistency is summarized in Table I.

IV. INTERFACIAL VELOCITY SLIP

As discussed in Sec. I, steady-state and stationary assumptions are commonly employed to simplify the high-order CE analysis of existing schemes. However, the applicability of these schemes under transient and moving conditions has not been thoroughly investigated. To address this limitation, two-phase Poiseuille flow and two-phase Couette flow are simulated in this section to evaluate the performance of existing schemes under moving conditions. The interfacial velocity slip phenomenon is observed during these simulations and a detailed discussion is provided.

A. Coexistence densities under moving conditions

To investigate whether velocity affects the coexistence densities, Table II presents a comparison of the coexistence densities for various schemes. The parameters used in the force schemes are consistent with those described in Sec. III B. The stationary results are obtained by simulating a one-dimensional flat plate, while the moving results are obtained from two-phase Poiseuille flow simulations. The specific settings for the Poiseuille flow simulations are detailed in Sec. IV B. For the McCracken-Abraham scheme, the operating temperature is set to $0.85T_c$, while for the other schemes, it is set to $0.70T_c$. The results under both stationary and moving conditions exhibit good agreement, indicating that velocity has minimal effect on the coexistence densities.

B. Two-phase Poiseuille flow

Two-phase Poiseuille flow serves as an effective test case for evaluating the applicability of force schemes under moving conditions. A schematic diagram of the two-phase Poiseuille flow is shown in Fig. 2(a). In this configuration, a two-phase fluid flows between two parallel plates, driven by a constant external force applied parallel to the plates. Due

TABLE II. Coexistence densities under stationary and moving conditions.

Force scheme	Stationary: ρ_{gas}	Moving: ρ_{gas}	Stationary: ρ_{liq}	Moving: ρ_{liq}
Shan-Chen [11]	7.196×10^{-3}	7.196×10^{-3}	8.076	8.076
EDM [25]	7.196×10^{-3}	7.196×10^{-3}	8.076	8.076
McCracken-Abraham [24]	6.279×10^{-2}	6.279×10^{-2}	6.547	6.547
Li *et al.*'s MRT [27]	6.280×10^{-2}	6.280×10^{-2}	8.080	8.081
Huang-Wu [29]	6.281×10^{-2}	6.281×10^{-2}	8.081	8.081
ST-EOS [31]	5.916×10^{-2}	5.916×10^{-2}	8.080	8.080

to the viscosity difference between the liquid and gas phases, the velocity profile deviates from the parabolic shape typically observed in single-phase Poiseuille flow.

In this study, the computational domain size is consistent with that described in Sec. III B. The external force $\boldsymbol{F}_{\text{ext}}$ is set to $(0, 10^{-7})^{\text{T}}$ and τ is fixed at 1. A periodic boundary condition is applied in the y direction, while no-slip boundary conditions are enforced at the left and right boundaries using the Zou-He boundary scheme [46]. The convergence criterion is defined as

$$\frac{\sqrt{\sum_{i,j=1}^{N_x,N_y}[u_y(i,j,t)-u_y(i,j,t-\delta_t)]^2}}{\sqrt{\sum_{i,j=1}^{N_x,N_y}[u_y(i,j,t-\delta_t)]^2}} < 10^{-9}, \tag{33}$$

where i and j represent the lattice indices in the x and y directions, respectively. For two-phase Poiseuille flow, the governing equations [Eqs. (1a), (1b), and (2)] can be simplified to

$$\frac{\partial}{\partial x}\left(\rho\nu\frac{\partial u_y}{\partial x}\right) = -F_{\text{ext,y}}. \tag{34}$$

The boundary conditions are given as $u_y(0, y) = 0$ and $u_y(L_x, y) = 0$. In this study, Eq. (34) is solved using the forward Euler method with a spatial step size of $0.1\delta_x$. The density $\rho(x)$ in Eq. (34) is obtained using cubic spline interpolation.

The velocity profiles for various density ratios are compared in Fig. 3. The density field is initialized using Eq. (32). For the Shan-Chen and EDM schemes, the temperature corresponding to a given density ratio is interpolated from the coexistence curve. For other schemes, the temperature is determined by the mechanical stability condition. As shown in Figs. 3(a), 3(b), 3(d), and 3(e), the calculated velocity profiles for the Shan-Chen, EDM, Li *et al.*'s MRT and Huang-Wu schemes agree well with the analytical solutions when $\rho_{\text{liq}}/\rho_{\text{gas}} = 5$. However, when $\rho_{\text{liq}}/\rho_{\text{gas}} = 10$, the calculated velocity profile slightly exceeds the analytical solution in the liquid region. At $\rho_{\text{liq}}/\rho_{\text{gas}} = 100$, significant discrepancies arise in the liquid region, where the velocity profile steeply rises at the liquid-gas interface, with the maximum velocity occurring at this interface. The same trend is observed in Fig. 3(f), but the overall deviation is relatively small. The reason is that for ST-EOS model, the interface thickness is always controlled at 10, which is relatively thick compared to other models. This phenomenon, where the velocity sharply changes at the liquid-gas interface, is referred to as interfacial velocity slip. In contrast, for the McCracken-Abraham scheme, the calculated velocity profiles are consistent with the analytical solutions across all density ratios, as shown in Fig. 3(c). The minor errors observed at high-density ratios are attributed to the thin interface thickness. Table I summarizes whether various schemes suffer from interfacial velocity slip.

The interface velocity slip phenomenon has been reported in previous work [47,48]. In many cases, it has been either overlooked or attributed to the effect of surface tension [47]. However, surface tension originates from the pressure tensor which, as shown in Eq. (34), has no direct impact on the velocity profile. This indicates that surface tension is not the root cause of this issue. The underlying mechanism behind interfacial velocity slip requires further in-depth investigation.

C. Two-phase Couette flow

Two-phase Couette flow is simulated to better capture interfacial velocity slip and evaluate the applicability of the

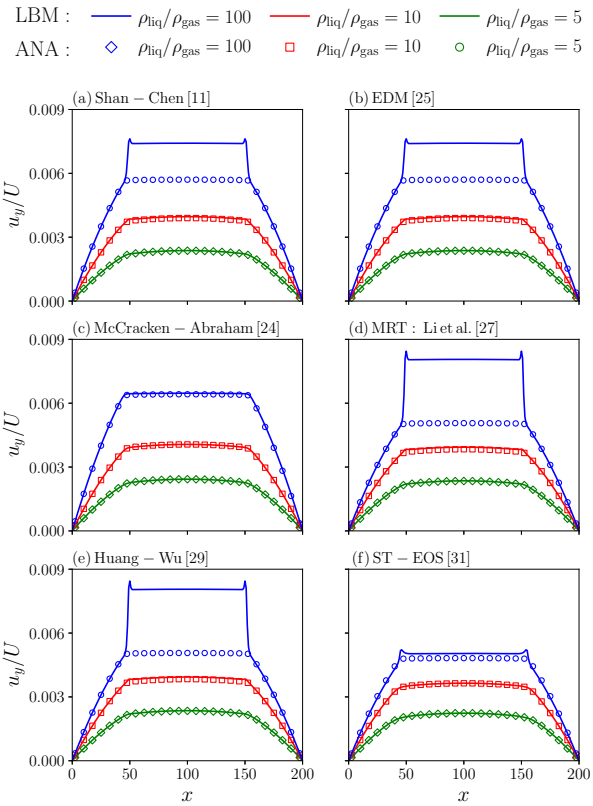

FIG. 3. Velocity profiles of two-phase Poiseuille flow for various force schemes. The results for $\rho_{\text{liq}}/\rho_{\text{gas}} = 100$ are scaled by a factor of 0.2.

schemes under moving conditions. A schematic diagram of the two-phase Couette flow is shown in Fig. 2(b). In this configuration, the external force is set to zero. The left boundary is treated as a no-slip wall, while the right boundary is assigned a constant velocity. In this study, the velocity at the right boundary is fixed at $U = 0.01$ in the y direction and 0 in the x direction. All other parameters are consistent with those described in Sec. IV B. The Zou-He boundary scheme [46] is employed to implement the constant velocity boundary condition.

Unlike two-phase Poiseuille flow, the density field for two-phase Couette flow is initialized as

$$\rho(\boldsymbol{x}) = \frac{\rho_{\text{liq}} + \rho_{\text{gas}}}{2} - \frac{\rho_{\text{liq}} - \rho_{\text{gas}}}{2} \tanh \frac{2(|x - L_x| - L_x/2)}{W}. \tag{35}$$

For Couette flow, the governing equations (1a) to (2) can be simplified to

$$\frac{\partial}{\partial x}\left(\rho \nu \frac{\partial u_y}{\partial x}\right) = 0. \tag{36}$$

The boundary conditions are $u_y(0, y) = 0$ and $u_y(L_x, y) = U$. A combination of the forward Euler and shooting methods is used to solve Eq. (36).

The velocity profiles of two-phase Couette flow for various force schemes are compared in Fig. 4. As shown in Figs. 4(a), 4(b), 4(d), and 4(e), the calculated results for the Shan-Chen, EDM, Li *et al.*'s MRT, and Huang-Wu schemes show good agreement with the analytical solutions when $\rho_{\text{liq}}/\rho_{\text{gas}} = 5$. However, when $\rho_{\text{liq}}/\rho_{\text{gas}} = 10$, the calculated velocity profile is slightly lower than the analytical solution in the gas region. At $\rho_{\text{liq}}/\rho_{\text{gas}} = 100$, significant discrepancies are observed in the gas region, where the velocity decreases steeply at the liquid-gas interface, with the maximum velocity occurring at the interface. This behavior is similar to that observed in two-phase Poiseuille flow. Meanwhile, the same trend is observed in Fig. 4(f) and the overall deviation is relatively small. In contrast, the McCracken-Abraham scheme produces a velocity profile consistent with the analytical solutions for all density ratios, as shown in Fig. 4(c). Unlike other schemes, the McCracken-Abraham scheme does not exhibit interfacial velocity slip, providing more reliable results in comparison to other schemes.

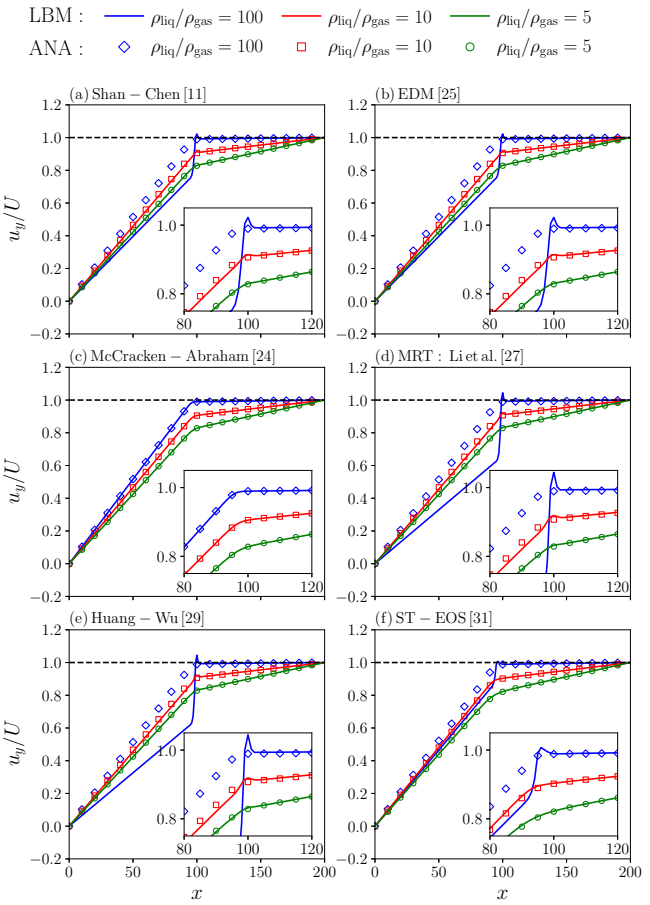

FIG. 4. Velocity profiles of two-phase Couette flow for various force schemes. Points represent the analytical solutions and solid lines represent the calculated results.

D. Discussion of the interfacial velocity slip mechanism

In this section, we explore the underlying causes of interfacial velocity slip in detail, starting with the shear stress τ_u and the reduced shear stress $\hat{\tau}_u$, which are defined as

$$\hat{\tau}_u = \frac{\tau_u - \tau_{u,\text{gas}}}{\tau_{u,\text{gas}}}, \quad \tau_u = \rho \nu \frac{\partial u_y}{\partial x}, \tag{37}$$

where $\tau_{u,\text{gas}}$ denotes the shear stress in the gas region. For Couette flow, Eq. (36) dictates that the shear stress remains constant, while the reduced shear stress should be zero.

Figure 5 illustrates the variation of the reduced shear stress for different density ratios. The simulation settings in Fig. 5 are the same as those in Fig. 4. By comparing Figs. 5(a), 5(b), and 5(d)–5(f), it is observed that $\hat{\tau}_u$ oscillates at the liquid-gas interface. Specifically, $\hat{\tau}_u$ is positive near the gas region and negative near the liquid region. Moreover, the oscillation amplitude increases with the density ratio. This oscillatory behavior explains the occurrence of the maximum velocity at the interface, as observed in Figs. 3 and 4. When the oscillation exceeds 1, $\hat{\tau}_u$ becomes less than -1, indicating that the shear stress is negative. This reversal in the shear stress leads to an inverted velocity gradient, resulting in the maximum velocity at the liquid-gas interface. In contrast, Fig. 5(c) shows that the McCracken-Abraham scheme exhibits minimal oscillation, with the maximum value of $\hat{\tau}_u$ being approximately 0.2. For comparison, the maximum value of $\hat{\tau}_u$ for the Huang-Wu scheme exceeds 300. These findings indicate that the shear stress oscillation is the intrinsic mechanism responsible for interfacial velocity slip.

What causes the shear stress oscillation? From Figs. 1, 3, and 4, it can be observed that the results of the Shan-Chen, EDM, Li *et al.*'s MRT and Huang-Wu schemes exhibit similar behavior. The similarity between the Shan-Chen and EDM schemes can be explained by the fact that the Shan-Chen scheme is equivalent to the EDM scheme when $\tau = 1$. Huang *et al.* [29,49] further pointed out that both the EDM and Li *et al.*'s MRT schemes can be expressed in the form of the Huang-Wu scheme. After mathematical derivation, the additional term in Li *et al.*'s MRT scheme, $\mathbf{Q}_{\mathbf{m}}^{\mathbf{Li}}$, can be expressed

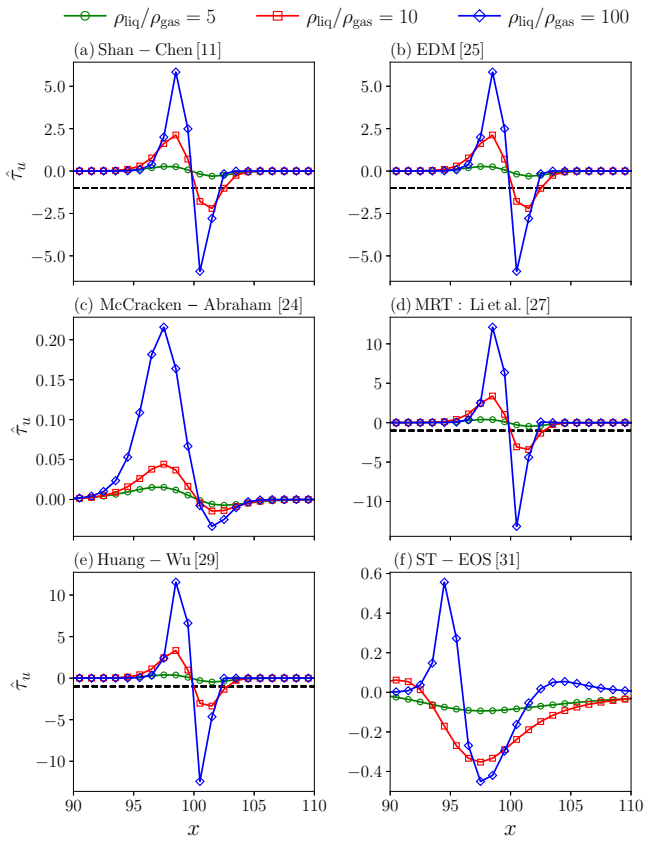

FIG. 5. Reduced shear stress for various density ratios. The results for $\rho_{liq}/\rho_{gas} = 100$ in panels (a), (b), and (d)–(f) are scaled by a factor of 1/30. Black dashed lines represent $\hat{\tau}_u = -1$.

as

$$\mathbf{Q}_{\mathbf{m}}^{\mathbf{Li}} = \left[0, 12G\sigma\frac{|\bar{\boldsymbol{F}}_{\mathbf{pp}}|^2}{G\psi^2}, -12G\sigma\frac{|\bar{\boldsymbol{F}}_{\mathbf{pp}}|^2}{G\psi^2}, 0, 0, 0, 0, 0, 0\right]. \tag{38}$$

The additional term in the EDM scheme given by Huang *et al.* [29,49] is expressed as

$$\mathbf{Q}_{\mathbf{m}}^{\mathbf{EDM}} = \left[0, \frac{3}{4}\frac{|\bar{\boldsymbol{F}}_{\mathbf{pp}}|^2}{\rho\delta_t^2}, -\frac{3}{4}\frac{|\bar{\boldsymbol{F}}_{\mathbf{pp}}|^2}{\rho\delta_t^2}, 0, 0, 0, 0, \frac{1}{4}\frac{(\bar{F}_{\mathrm{pp},x}^2 - \bar{F}_{\mathrm{pp},y}^2)}{\rho\delta_t^2}, \frac{1}{4}\frac{\bar{F}_{\mathrm{pp},x}\bar{F}_{\mathrm{pp},y}}{\rho\delta_t^2}\right]^{\mathrm{T}}. \tag{39}$$

By comparing Eqs. (29) and (38), it can be seen that Li *et al.*'s scheme is a special case of the Huang-Wu scheme with $k_1 = 0$ and $k_2 = 2G\sigma$. Similarly, by comparing Eqs. (29) and (39), the EDM scheme is identified as a variant of the Huang-Wu scheme with $k_1 = 1/4$ and $k_2 = 0$. Additionally, ψ^2 in Eq. (29) is replaced by $\rho\delta_t^2$, which explains the appearance of the term ψ^2/ρ in the ϵ for EDM scheme. Moreover, the ST-EOS model also includes the additional term $\mathbf{\Lambda Q_m}$ in the collision step. The only difference between the Huang-Wu and McCracken-Abraham schemes lies in the additional term. Thus, the additional term $\mathbf{\Lambda Q_m}$ plays a crucial role in the observed interfacial velocity slip and shear stress oscillation.

To investigate the origin of interfacial velocity slip resulting from $\mathbf{Q_m}$, we first need to examine the CE expansion of the McCracken-Abraham scheme. Begin by performing a Taylor expansion of Eq. (15):

$$\delta_t \boldsymbol{D}_i f_i + \frac{\delta_t^2}{2}(\boldsymbol{D}_i)^2 f_i + O(\delta_t^3) = f_i^*(\boldsymbol{x}, t), \tag{40}$$

where $\boldsymbol{D}_i = (\partial_t + \boldsymbol{e}_i \cdot \boldsymbol{\nabla})$. Next, consider Eq. (23), we convert Eq. (40) to momentum space:

$$\mathbf{Dm} + \frac{\delta_t}{2}(\mathbf{D})^2\mathbf{m} + O(\delta_t^2) = -\frac{\mathbf{\Lambda}}{\delta_t}(\mathbf{m} - \mathbf{m^{eq}}) + \left(\mathbf{I} - \frac{\mathbf{\Lambda}}{2}\right)\mathbf{F}, \tag{41}$$

where $\mathbf{D} = \mathbf{I}\partial_t + \mathbf{M}[\mathrm{diag}(\boldsymbol{e}_0 \cdot \boldsymbol{\nabla}, \ldots, \boldsymbol{e}_8 \cdot \boldsymbol{\nabla})]\mathbf{M}^{-1}$. For the CE expansion, the following rules apply:

$$\partial_t = \sum_{n=1}^{+\infty}\varepsilon^n\partial_{tn}, \quad \boldsymbol{\nabla} = \varepsilon\boldsymbol{\nabla}_1, \quad \mathbf{f} = \sum_{n=0}^{+\infty}\varepsilon^n\mathbf{f^{(n)}}, \quad \boldsymbol{F} = \varepsilon\boldsymbol{F}^{(1)}, \tag{42}$$

where ε is the small expansion parameter. The following equations can be derived from Eq. (42):

$$\mathbf{m} = \sum_{n=0}^{+\infty}\varepsilon^n\mathbf{m^{(n)}}, \quad \mathbf{F_m} = \varepsilon\mathbf{F_m}^{(1)}. \tag{43}$$

Substituting Eqs. (42) and (43) into Eq. (41) and comparing the order of ε yields

$$\varepsilon^0 : \quad \mathbf{m}^{(0)} = \mathbf{m^{eq}}, \tag{44a}$$

$$\varepsilon^1 : \quad \mathbf{D}_1\mathbf{m}^{(0)} - \mathbf{F}_{\mathbf{m}}^{(1)} = -\frac{\mathbf{\Lambda}}{\delta_t}\left(\mathbf{m}^{(1)} + \frac{\delta_t}{2}\mathbf{F}_{\mathbf{m}}^{(1)}\right), \tag{44b}$$

$$\varepsilon^2 : \quad \partial_{t2}\mathbf{m}^0 + \mathbf{D}_1\mathbf{m}^{(1)} + \frac{\delta_t}{2}\mathbf{D}_1^2\mathbf{m}^{(0)} = -\frac{\mathbf{\Lambda}}{\delta_t}\mathbf{m}^{(2)}, \tag{44c}$$

where $\mathbf{D}_1 = \mathbf{I}\partial_{t1} + \mathbf{M}[\mathrm{diag}(\boldsymbol{e}_0 \cdot \boldsymbol{\nabla}_1, \ldots, \boldsymbol{e}_8 \cdot \boldsymbol{\nabla}_1)]\mathbf{M}^{-1}$. Equation (44c) can be simplified using Eq. (44b):

$$\varepsilon^2 : \ \partial_{t2}\mathbf{m}^{(0)} + \mathbf{D}_1\left(\mathbf{I} - \frac{\mathbf{\Lambda}}{2}\right)\left(\mathbf{m}^{(1)} + \frac{\delta_t}{2}\mathbf{F}_{\mathbf{m}}^{(1)}\right) = -\frac{\mathbf{\Lambda}}{\delta_t}\mathbf{m}^{(2)}. \tag{45}$$

Combining Eqs. (16) and (22) gives $m_0 = \rho$, $m_3 = \rho\bar{u}_x - \delta_t\bar{F}_x/2$ and $m_5 = \rho\bar{u}_y - \delta_t\bar{F}_y/2$. Therefore, the following equations can be derived from Eq. (44a):

$$m_0^{(1)} + \tfrac{\delta_t}{2}F_{\mathrm{m}0}^{(1)} = 0, \quad m_0^{(\mathrm{n})} = 0(\forall n \geqslant 2), \tag{46a}$$

$$m_3^{(1)} + \tfrac{\delta_t}{2}F_{\mathrm{m}3}^{(1)} = 0, \quad m_3^{(\mathrm{n})} = 0(\forall n \geqslant 2), \tag{46b}$$

$$m_5^{(1)} + \tfrac{\delta_t}{2}F_{\mathrm{m}5}^{(1)} = 0, \quad m_5^{(\mathrm{n})} = 0(\forall n \geqslant 2). \tag{46c}$$

Considering Eqs. (26) and (46), expanding the zeroth, third, and fifth components of Eq. (44b) yields

$$\partial_{t1}\rho + \partial_{x1}(\rho u_x) + \partial_{y1}(\rho u_y) = 0, \tag{47a}$$

$$\partial_{t1}(\rho u_x) + \partial_{x1}\left(\rho u_x^2\right) + \partial_{y1}(\rho u_x u_y) = -\partial_{x1}\left(\rho c_s^2\right) + F_x^{(1)}, \tag{47b}$$

$$\partial_{t1}(\rho u_y) + \partial_{x1}(\rho u_x u_y) + \partial_{y1}\left(\rho u_y^2\right) = -\partial_{y1}\left(\rho c_s^2\right) + F_y^{(1)}. \tag{47c}$$

Similarly, expanding the zerord, third, and fifth components of Eq. (45) yields

$$\partial_{t2} m_0^{(0)} + \partial_{t1} \bar{m}_0^{(1)} + c\partial_{x1} \bar{m}_3^{(1)} + c\partial_{y1} \bar{m}_5^{(1)} = 0, \tag{48a}$$

$$\partial_{t2} m_3^{(0)} + \partial_{t1} \bar{m}_3^{(1)} + c\partial_{x1}\left(\tfrac{2}{3}\bar{m}_0^{(1)} + \tfrac{1}{6}\bar{m}_1^{(1)} + \tfrac{1}{2}\bar{m}_7^{(1)}\right) + c\partial_{y1}\bar{m}_8^{(1)} = 0, \tag{48b}$$

$$\partial_{t2} m_5^{(0)} + \partial_{t1} \bar{m}_5^{(1)} + c\partial_{x1}\bar{m}_8^{(1)} + c\partial_{y1}\left(\tfrac{2}{3}\bar{m}_0^{(1)} + \tfrac{1}{6}\bar{m}_1^{(1)} - \tfrac{1}{2}\bar{m}_7^{(1)}\right) = 0, \tag{48c}$$

where $\bar{m}_i^{(1)} = [1 - 1/(2\tau_i)](m_i^{(1)} + \delta_t F_{\mathrm{m}i}^{(1)})/2$. Here, τ_i represents the ith component of $\mathbf{\Lambda}$. Equation (46) indicates that $m_0^{(1)} = m_3^{(1)} = m_5^{(1)} = 0$. The components $m_1^{(1)}$, $m_7^{(1)}$ and $m_8^{(1)}$ can be derived from Eq. (44b), yielding the following equations:

$$-\frac{1}{\delta_t \tau_1}\left(m_1^{(1)} + \tfrac{\delta_t}{2}F_{\mathrm{m1}}^{(1)}\right) \approx 2\rho\partial_{x1}u_x + 2\rho\partial_{y1}u_y, \tag{49a}$$

$$-\frac{1}{\delta_t \tau_7}\left(m_7^{(1)} + \tfrac{\delta_t}{2}F_{\mathrm{m7}}^{(1)}\right) \approx \frac{2}{3}\rho\partial_{x1}\bar{u}_x - \frac{2}{3}\rho\partial_{y1}(\bar{u}_y), \tag{49b}$$

$$-\frac{1}{\delta_t \tau_8}\left(m_8^{(1)} + \tfrac{\delta_t}{2}F_{\mathrm{m8}}^{(1)}\right) \approx \frac{1}{3}\rho\partial_{x1}(\bar{u}_y) + \frac{1}{3}\rho\partial_{y1}(\bar{u}_x), \tag{49c}$$

where "≈" denotes the neglect of the cubic term in the velocity. Substituting Eq. (49) into Eq. (48) yields

$$\partial_{t2}\rho = 0, \tag{50a}$$

$$\partial_{t2}(\rho u_x) = \partial_{x1}[\eta(\partial_{x1}u_x - \partial_{y1}u_y) + \xi(\partial_{x1}u_x + \partial_{y1}u_y)] + \partial_{y1}[\eta(\partial_{y1}u_x + \partial_{x1}u_y)], \tag{50b}$$

$$\partial_{t2}(\rho u_y) = \partial_{x1}[\eta(\partial_{x1}u_y + \partial_{y1}u_x)] + \partial_{y1}[\eta(\partial_{y1}u_y - \partial_{x1}u_x) + \xi(\partial_{x1}u_x + \partial_{y1}u_y)], \tag{50c}$$

where $\eta = \rho c_s^2 \delta_t(\tau_v - 1/2)$ and $\xi = \rho c_s^2 \delta_t(\tau_\xi - 1/2)$. Combining Eqs. (47) and (50), we obtained the macroscopic equations for the McCracken-Abraham scheme:

$$\partial_t \rho + \nabla \cdot (\rho \boldsymbol{u}) = 0, \tag{51a}$$

$$\partial_t(\rho \boldsymbol{u}) + \nabla \cdot (\rho \boldsymbol{u}\boldsymbol{u}) = -\nabla p + \boldsymbol{F} + \nabla\{\eta[\nabla \boldsymbol{u} + (\nabla \boldsymbol{u})^{\mathrm{T}} - (\nabla \cdot \boldsymbol{u})\mathbf{I}]\} + \nabla(\xi \nabla \cdot \boldsymbol{u}). \tag{51b}$$

When τ_ξ and τ_v are equal, the macroscopic equations of McCracken-Abraham scheme become identical to those of Guo *et al.*'s scheme [23].

From the above analysis, it is evident that lower-order ε terms are used when deriving the macroscopic equations for higher-order ε terms. For instance, Eq. (44a) is utilized to simplify Eq. (44b), while Eq. (44b) is used to simplify Eq. (44c) and to derive $m_1^{(1)}$, $m_7^{(1)}$ and $m_8^{(1)}$, which play a crucial role in the second-order macroscopic equations. It is observed that the additional term in Eq. (29) is a second-order ε terms. The zeroth, third, fourth, fifth, and sixth components are constrained to zero due to mass and momentum conservation. Consequently, $\mathbf{Q_m}$ does not influence the second-order macroscopic equations, i.e., the Navier-Stokes equations. However, $\mathbf{Q_m}$ introduces additional terms into the third-order macroscopic equations. Previous studies have achieved thermodynamic consistency using these additional terms [28,29,44]. However, these studies only considered terms unrelated to velocity and time. To the best of our knowledge, no third- or fourth-order CE analysis has been performed on any force scheme without simplifications. All existing analyses rely on steady-state and stationary assumptions to simplify high-order CE analysis, ignoring additional terms related to time derivatives and velocity.

We hypothesize that $\mathbf{Q_m}$ introduces a third-order ε term related to force and velocity. For the Shan-Chen scheme, the conjectured additional term in the y-momentum equation takes the form $\partial_x[C_1\partial_x(F_x u_y u_y)]$, which is a third-order ε term. Figure 6(a) compares $\tau_u - \tau_{u,\mathrm{gas}}$ and $C_1\partial_x(F_x u_y u_y)$. It is evident that, when the constant C_1 is set to 2, both trends show good agreement. The strong correlations observed in Fig. 6 support our hypothesis that the third-order ε term related to force and velocity is the underlying cause of shear stress oscillation and interfacial velocity slip.

It is important to emphasize that the additional terms shown in Fig. 6 are conjectural. The actual additional terms can be derived through a third-order CE expansion. However, performing high-order CE analysis on a force scheme without simplifications is extremely challenging, and to date, no such analysis has been conducted. Only a few higher-order CE analyses have been conducted for simpler models, such as the Cahn-Hilliard equation [50] and the D2Q9-MRT model without a force scheme [51]. It has been observed that the error terms causing the shear stress oscillation appear to be independent of time. This raises the question of whether steady-state assumptions could be adopted to simplify the analysis. Unfortunately, steady CE analysis is only valid under incompressible conditions [39]. Silva and Semião [52] conducted fourth-order steady CE analyses on the D3Q15, D3Q19 and D3Q27 models. Their results indicate that the stress tensor obtained from steady CE analysis is given by $\mathbf{\Pi} = \nu[\nabla(\rho \boldsymbol{u}) + \nabla(\rho \boldsymbol{u})^{\mathrm{T}}]$, which is valid only when ρ is constant. However, the compressibility of the LB model is precisely what the pseudopotential model exploits. As a result, applying steady CE analysis to a force scheme would lead to erroneous conclusions.

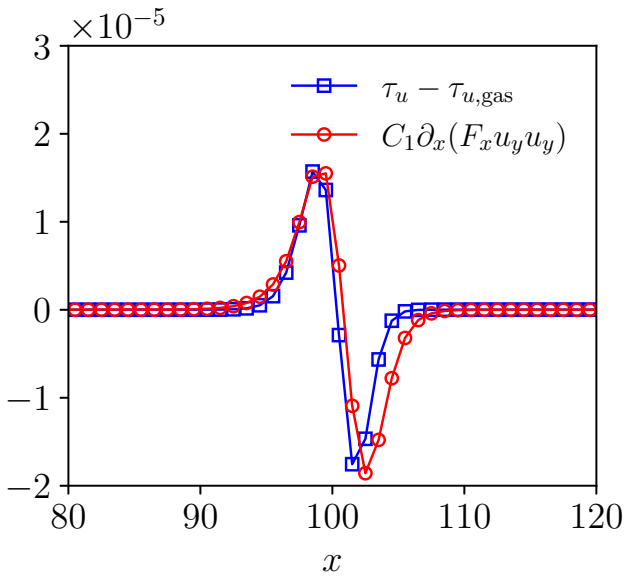

FIG. 6. Variation of $\tau_u - \tau_{u,\mathrm{gas}}$ and conjectured additional term $C_1\partial_x(F_x u_y u_y)$ for two-phase Couette flow, where C_1 is taken as 2. The force scheme is Shan-Chen scheme and the density ratio is 10.

V. NEW PSEUDOPOTENTIAL FORCE FOR ELIMINATING INTERFACIAL VELOCITY SLIP

How can a pseudopotential model be developed to adjust coexistence densities while eliminating interfacial velocity slip? Theoretically, a third-order analysis could be applied to the McCracken-Abraham scheme, allowing for the selection of an appropriate $\mathbf{Q_m}$ to adjust the coexistence densities. However, this approach is a mathematical problem rather than a physical one and is inherently complex. Therefore, we have chosen not to address the problem in this manner.

Instead, two promising schemes can be considered: Guo *et al.*'s scheme and the McCracken-Abraham scheme. Huang and Wu [29] conducted a third-order CE analysis on the McCracken-Abraham scheme and found that the additional term for this scheme can be expressed as

$$\boldsymbol{R}_{\mathbf{iso}} = \frac{\delta_x^2}{12}\nabla\cdot\nabla\boldsymbol{F}. \tag{52}$$

The same result was derived by Wu *et al.* [38]. Although their analysis also relied on steady-state and stationary assumptions, the numerical results presented in Figs. 3–5 suggest that $\boldsymbol{R}_{\mathbf{iso}}$ is the only additional term for the McCracken-Abraham scheme. This is an encouraging finding.

A. Introduction to our model

The coexistence densities are inherently related to the pressure tensor, which is governed by the pseudopotential force. Therefore, the coexistence densities can be adjusted via modifications to the pseudopotential force. For instance, consider the term $\nabla\psi\cdot\nabla\psi$ from the pressure tensor [Eq. (9)]; the corresponding force is given by $\nabla(\nabla\psi\cdot\nabla\psi)$. It is evident that this term cannot be explicitly discretized in two-dimensional cases using a nine-point stencil. The same issue arises for other components of the pressure tensor. Fortunately, the following identity is observed:

$$2\nabla^2\psi\nabla\psi = \nabla\cdot[2\nabla\psi\nabla\psi - (\nabla\psi\cdot\nabla\psi)\mathbf{I}]. \tag{53}$$

The left-hand side of Eq. (53) can be explicitly discretized using a nine-point stencil in two-dimensional cases. Based on this identity, we propose a new pseudopotential force:

$$\boldsymbol{F}_{\mathbf{new}}(\boldsymbol{x}) = -G\psi\tilde{\nabla}\psi - 2\gamma\tilde{\nabla}^2\psi\tilde{\nabla}\psi, \tag{54}$$

where

$$\tilde{\nabla}\psi = \frac{1}{\delta_x}\sum_i w_i\psi(\boldsymbol{x}+\boldsymbol{e_i}\delta_t)\frac{\boldsymbol{e_i}}{c}, \tag{55a}$$

$$\tilde{\nabla}^2\psi = \frac{2}{\delta_x^2}\sum_i w_i[\psi(\boldsymbol{x}+\boldsymbol{e_i}\delta_t)-\psi(\boldsymbol{x})]. \tag{55b}$$

Here, γ is a parameter used to adjust the liquid-gas coexistence densities, w_i represents $w(|\boldsymbol{e_i}/c|^2)$. $\tilde{\nabla}\psi$ and $\tilde{\nabla}^2\psi$ are the discrete forms of $\nabla\psi$ and $\nabla^2\psi$, respectively. Taylor expansion of Eq. (54) at poistion $\boldsymbol{x}$ yields

$$\boldsymbol{F}_{\mathbf{new}} = -G\psi\nabla\psi - \kappa_{\mathrm{new}}\psi\nabla\nabla\cdot\nabla\psi - 2\gamma\nabla^2\psi\nabla\psi. \tag{56}$$

Here, $\kappa_{\mathrm{new}} = G\delta_x^2/6$ and higher-order terms of $O(\nabla^5)$ are neglected. When Guo *et al.*'s and McCracken-Abraham schemes are employed and considering the error term $\boldsymbol{R}_{\mathbf{iso}}$, the actual pseudopotential force in our model is expressed as

$$\begin{aligned}\boldsymbol{F}_{\mathbf{our}} &= \boldsymbol{F}_{\mathbf{new}} + \boldsymbol{R}_{\mathbf{iso}}\\ &= -G\psi\nabla\psi - \kappa_{\mathrm{new}}\psi\nabla\nabla\cdot\nabla\psi\\ &\quad - 2\gamma\nabla^2\psi\nabla\psi - \frac{\kappa_{\mathrm{new}}}{4}\nabla\cdot\nabla\nabla\psi^2.\end{aligned} \tag{57}$$

The following equation holds [29]:

$$\begin{aligned}\nabla\nabla\cdot\nabla\psi^2 = 2\nabla\cdot[&b_1(\nabla\psi\nabla\psi+\psi\nabla\nabla\psi)\\ &+ b_2(\nabla\psi\cdot\nabla\psi+\psi\nabla^2\psi)\mathbf{I}].\end{aligned} \tag{58}$$

The free parameters b_1 and b_2 satisfy the condition $b_1 + b_2 = 1$. Considering Eqs. (7), (53), and (58), the corresponding pressure tensor of our pseudopotentia force is given as follows:

$$\begin{aligned}\mathbf{P}_{\mathbf{our}} = &\frac{G}{2}\psi^2\mathbf{I} + \frac{\kappa_{\mathrm{new}}}{2}\{[b_2\nabla\psi\cdot\nabla\psi + b_2\psi\nabla^2\psi]\mathbf{I}\\ &+ b_1\nabla\psi\nabla\psi + b_1\psi\nabla\nabla\psi\} + \kappa_{\mathrm{new}}\{[a_3\nabla\psi\cdot\nabla\psi\\ &+ a_4\psi\nabla^2\psi]\mathbf{I} + a_1\nabla\psi\nabla\psi + a_2\psi\nabla\nabla\psi\}\\ &+ [-\gamma\nabla\psi\cdot\nabla\psi]\mathbf{I} + 2\gamma\nabla\psi\nabla\psi.\end{aligned} \tag{59}$$

The total pressure tensor is given by $\mathbf{P} = p_{\mathrm{LBE}}\mathbf{I} + \mathbf{P}_{\mathbf{our}}$. At this stage, the pseudopotential needs to satisfy the following

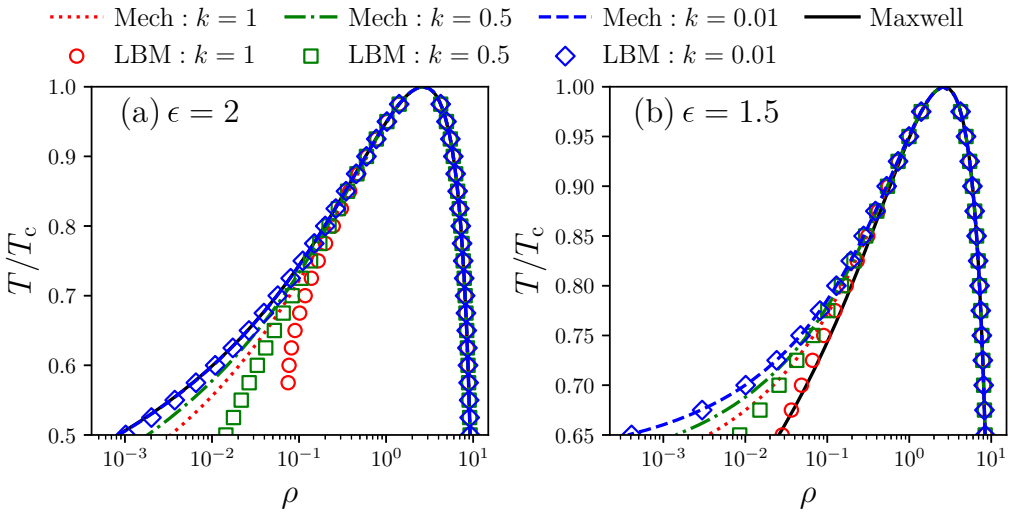

FIG. 7. Coexistence densities of our model for (a) $\epsilon = 2$ and (b) $\epsilon = 1.5$.

form:

$$\psi = \sqrt{\frac{2\left(p_{\mathrm{EOS}}^{\mathrm{new}} - p_{\mathrm{LBE}}\right)}{G}}, \tag{60}$$

where $p_{\mathrm{EOS}}^{\mathrm{new}} = k p_{\mathrm{EOS}}$. The parameter k can be used to adjust the liquid-gas interface thickness [35,36]. For a one-dimensional flat plate problem, the normal pressure is given as follows:

$$P_{\mathrm{n}} = p_{\mathrm{EOS}}^{\mathrm{new}} + \frac{\kappa_{\mathrm{new}}}{2}\left[\frac{2\gamma}{\kappa_{\mathrm{new}}}\left(\frac{\mathrm{d}\psi}{\mathrm{d}x}\right)^2 + 3\psi\frac{\mathrm{d}^2\psi}{\mathrm{d}x^2}\right]. \tag{61}$$

Referring to Appendix A in Ref. [27], Eq. (11) can be rewritten as

$$(P_{\mathrm{n}} - p_{\mathrm{EOS}})\frac{\psi'}{\psi^{1+\epsilon}} = \frac{3\kappa_{\mathrm{pp}}}{4}\frac{\mathrm{d}}{\mathrm{d}\rho}\left[\frac{(\psi')^2}{\psi^{\epsilon}}\left(\frac{\mathrm{d}\rho}{\mathrm{d}x}\right)^2\right]. \tag{62}$$

Here, the parameter ϵ for our model is

$$\epsilon = -\frac{4\gamma}{3\kappa_{\mathrm{new}}} = -\frac{8\gamma}{G\delta_x^2}. \tag{63}$$

The density profiles can also be derived from Eq. (62). Integrating Eq. (62) from ρ_{gas} to ρ, we obtain

$$\left(\frac{\mathrm{d}\rho}{\mathrm{d}x}\right)^2 = \frac{4\psi^{\epsilon}}{3\kappa_{\mathrm{pp}}(\psi')^2}\int_{\rho_{\mathrm{gas}}}^{\rho}(p_{\mathrm{EOS}} - P_{\mathrm{n}})\frac{\psi'}{\psi^{1+\epsilon}}\,\mathrm{d}\rho. \tag{64}$$

In this study, the density profile is computed by solving Eq. (64) using the forward Euler method with a sufficiently small spatial step.

Compared with other models that satisfy thermodynamic consistency, our model has the following advantages:

(i) *Switch easily between SRT and MRT*

The MRT model is well-known for its superior numerical stability compared to the SRT model, which, in contrast, offers advantages in computational simplicity and ease of implementation. Although other models can be derived by the space transformation to produce the corresponding SRT or MRT versions, but the derivation process is still necessary. Therefore, Huang-Wu scheme and ST-EOS model still lacks their SRT versions. In contrast, our model introduces changes only to the pseudopotential force, allowing seamless compatibility with both the SRT (Guo *et al.*'s scheme) and MRT (McCracken-Abraham scheme) models without requiring additional adjustments. Meanwhile, theoretically our model can also be easily extended to advanced central moment models [53]. It is sufficient to implant the proposed pseudopotential force into the corresponding central moment model [54] of the Guo *et al.*'s force scheme. The related work will be done in the future.

(ii) *Clear physical interpretation*

In our model, the coexistence densities are adjustable through modifications to the pressure tensor, which is determined by the pseudopotential force. By incorporating an additional term, $2\gamma\tilde{\nabla}^2\psi\tilde{\nabla}\psi$, into the pseudopotential force, We can effectively adjust the coexistence densities to achieve thermodynamic consistency. This adjustment provides a clearer and more intuitive physical interpretation compared to other models that satisfy thermodynamic consistency. From Eqs. (21), (28), and (29), it can be found that the corrections to Guo et al's scheme or McCracken-Abraham scheme in these schemes are unfavorable for understanding.

(iii) *Adjustable coexistence densities with no interfacial velocity slip*

Most existing models [11,25–27,29,31] suffer from interfacial velocity slip. While other models [23,24] do not satisfy thermodynamic consistency. Our model overcomes these limitations by enabling the adjustment of coexistence densities while eliminating interfacial velocity slip. This feature represents a significant advancement and a key advantage of our model.

Although the models proposed by previous researchers have certain limitations, their work and ideas form the foundation of our model. We deeply appreciate their contributions in advancing pseudopotential models.

B. Coexistence densities and interface thickness

Figure 7 illustrates the coexistence densities of our model. In this section, the domain length L_x is a function of k, given

by $L_x = 200/\sqrt{k}$, and the initial interface thickness W_{init} also varies with k, expressed as $W_{\text{init}} = 5/\sqrt{k}$. Other parameters are consistent with those described in Sec. III B. The results show that k influences the coexistence densities, particularly the gas density, which decreases as k reduces, while the effect on the liquid density is relatively minor. Additionally, a larger density ratio is achieved as k decreases. For instance, at $k = 1$, the maximum density ratio obtained from the LBM is around 10^2, but when $k = 0.01$, this ratio easily reaches 10^4. This phenomenon can be attributed to the increase in interface thickness as k decreases, a trend that has been reported in previous studies [27,31,35–37]. However, the underlying physical mechanism behind the interface thickening remains unclear.

It can be observed that the nature of decreasing k corresponds to a decrease in pressure. However, the pressure in physical units does not change. To better understand the physical mechanism behind the interface thickening, we perform a unit conversion. As is well known, the conversion between lattice units and physical units satisfies $\mathrm{L}_{\text{phys}} = \mathrm{L}_{\text{conv}} \cdot \mathrm{L}_{\text{latt}}$, $\mathrm{M}_{\text{phys}} = \mathrm{M}_{\text{conv}} \cdot \mathrm{M}_{\text{latt}}$, $\mathrm{T}_{\text{phys}} = \mathrm{T}_{\text{conv}} \cdot \mathrm{T}_{\text{latt}}$, where L represents length, M represents mass, T represents time, 'phys' refers to physical units, 'latt' refers to lattice units and 'conv' refers to the conversion coefficient. Using density, pressure, and kinematic viscosity as basic parameters, the following equations can be derived:

$$\begin{aligned} \rho_{\text{conv}} &= \rho_{\text{phys}}/\rho_{\text{latt}} = \mathrm{M}_{\text{conv}}/\mathrm{L}_{\text{conv}}^3, \\ p_{\text{conv}} &= p_{\text{phys}}/p_{\text{latt}} = \mathrm{M}_{\text{conv}}/\left(\mathrm{L}_{\text{conv}}\mathrm{T}_{\text{conv}}^2\right), \\ \nu_{\text{conv}} &= \nu_{\text{phys}}/\nu_{\text{latt}} = \mathrm{L}_{\text{conv}}^2/\mathrm{T}_{\text{conv}}. \end{aligned} \tag{65}$$

Solving Eq. (65) yields

$$\begin{aligned} \mathrm{L}_{\text{conv}} &= \sqrt{\frac{\rho_{\text{conv}}\nu_{\text{conv}}^2}{p_{\text{conv}}}}, \\ \mathrm{T}_{\text{conv}} &= \frac{\rho_{\text{conv}}\nu_{\text{conv}}}{p_{\text{conv}}}, \\ \mathrm{M}_{\text{conv}} &= \frac{\rho_{\text{conv}}^{2.5}\nu_{\text{conv}}^3}{p_{\text{conv}}^{1.5}}. \end{aligned} \tag{66}$$

When k is introduced, p_{conv} is replaced by p_{conv}/k. Consequently, the following equations hold:

$$\mathrm{L}_{\text{conv}}^k = \sqrt{k}\,\mathrm{L}_{\text{conv}}, \quad \mathrm{T}_{\text{conv}}^k = k\,\mathrm{T}_{\text{conv}}, \quad \mathrm{M}_{\text{conv}}^k = k^{1.5}\,\mathrm{M}_{\text{conv}}. \tag{67}$$

Here, the superscript k denotes the conversion coefficient considering k. From Eq. (67), it is evident that when using $p_{\text{EOS}}^{\text{new}}$, the spatial step δ_x in physical units becomes $\sqrt{k}$ times the spatial step used with p_{EOS}. As a result, the interface thickness in lattice units increases as k decreases.

Figure 8 shows the variations of ρ and $\partial_x\rho/\sqrt{k}$ with $x/\sqrt{k}$. It can be observed that as k decreases, the number of lattice points in the interface increases, while the interface thickness in physical units remains largely unchanged. These results indicate that k primarily affects the interface thickness in lattice units, while the thickness in physical units remains constant. The effect of k is essentially equivalent to multiplying the spatial step in physical units by $\sqrt{k}$. This conclusion explains the findings of Li *et al.* [27], where the interface thickness is

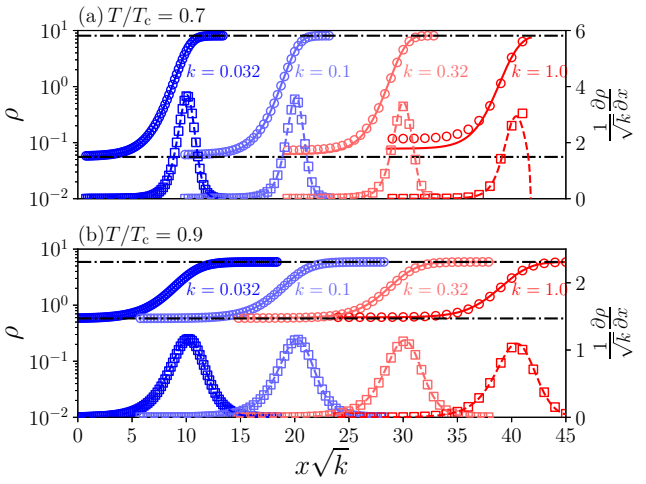

FIG. 8. Variations of ρ and $\partial_x\rho/\sqrt{k}$ with $x\sqrt{k}$. Circle points represent the calculated results of ρ. Solid lines represent the analytical solutions of ρ. Dash-dotted lines represent the coexistence densities given by Maxwell construction. Dashed lines represent the analytical solutions of $\partial_x\rho/\sqrt{k}$. Square points represent the calculated results of $\partial_x\rho/\sqrt{k}$. ϵ is taken as 2.

shown to be proportional to $1/\sqrt{a}$. In the context of the C-S EOS, the parameter a has an effect equivalent to that of k. Furthermore, Fig. 8 also reveals that $\partial_x\rho/\sqrt{k}$ becomes narrower and taller as k decreases, which leads to larger errors and ultimately results in computational dispersion. This behavior explains why achieving large density ratios is particularly challenging.

It is worth noting that in Figs. 7 and 8, the coexistence densities for $\epsilon = 2$ show better agreement with the Maxwell construction as k decreases. Previous studies have indicated that the optimal value of ϵ is approximately 2. For instance, the best-fitting ϵ in Fig. 1 is 1.8, while Li *et al.* report optimal values of 1.68 [26] and 1.76 [27]. Huang and Wu [29] also observed that $\epsilon = 2$ provides good agreement with the Maxwell construction. This phenomenon can be explained by taking the limit of Eq. (13) as $k \to 0$. When $k \to 0$, the following relations are obtained (with $G = -1$):

$$\lim_{k\to 0}\psi = \sqrt{2\rho c_s^2}, \quad \lim_{k\to 0}\psi' = \frac{c_s^2}{\sqrt{2\rho c_s^2}}. \tag{68}$$

Substituting Eq. (68) into Eq. (13) yields

$$\int_{\rho_{\text{gas}}}^{\rho_{\text{liq}}} (P_{\text{n}} - p_{\text{EOS}})\frac{1}{\rho^{(2+\epsilon)/2}}\,\mathrm{d}\rho = 0. \tag{69}$$

By comparing Eq. (69) with Eq. (5), it is clear that when $\epsilon = 2$, the two equations are equivalent. This explains the good agreement between the results for $\epsilon = 2$ and the Maxwell construction. To facilitate comparison, we define $\mathrm{Diff}_{\text{gas}}$ and $\mathrm{Diff}_{\text{liq}}$ to quantify the difference between the coexistence densities and those given by the Maxwell construction:

$$\mathrm{Diff}_{\text{gas}} = \frac{\rho_{\text{gas}} - \rho_{\text{gas}}^{\text{Max}}}{\rho_{\text{gas}}^{\text{Max}}}, \quad \mathrm{Diff}_{\text{liq}} = \frac{\rho_{\text{liq}} - \rho_{\text{liq}}^{\text{Max}}}{\rho_{\text{liq}}^{\text{Max}}}, \tag{70}$$

where $\rho_{\text{gas}}^{\text{Max}}$ and $\rho_{\text{liq}}^{\text{Max}}$ represent the gas and liquid densities, respectively, as given by the Maxwell construction. Figure 9

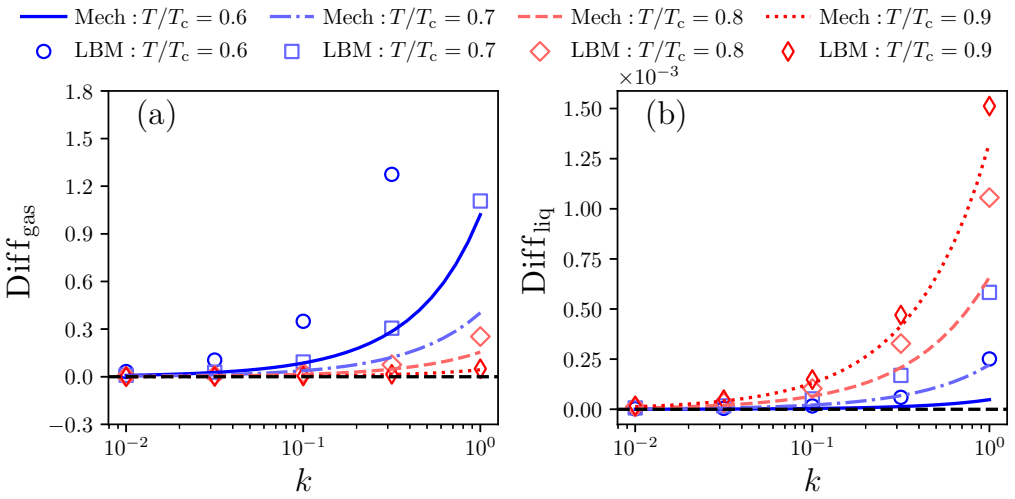

FIG. 9. Variations of (a) $\mathrm{Diff}_{\mathrm{gas}}$ and (b) $\mathrm{Diff}_{\mathrm{liq}}$ with k for $\epsilon = 2$.

shows the variations of $\mathrm{Diff}_{\mathrm{gas}}$ and $\mathrm{Diff}_{\mathrm{liq}}$ with k for $\epsilon = 2$. The results indicate that $\mathrm{Diff}_{\mathrm{gas}}$ and $\mathrm{Diff}_{\mathrm{liq}}$ are always positive, suggesting that the coexistence densities for $\epsilon = 2$ are consistently higher than those given by the Maxwell construction. This explains why the best-fitting ϵ is typically lower than 2. As shown in Fig. 7, the gas density decreases as ϵ decreases, which can counteract the effect of $p_{\mathrm{EOS}} > 0$. Moreover, the error between the LBM results and the mechanical stability becomes smaller as k decreases, consistent with the findings in Figs. 7 and 8. Additionally, both $\mathrm{Diff}_{\mathrm{gas}}$ and $\mathrm{Diff}_{\mathrm{liq}}$ gradually converge to 0 as k decreases, which aligns with the conclusion drawn from taking the limit.

C. $\mathbf{Q_m}$ corresponding to our model

As discussed at the beginning of Sec. V, we can perform a third-order analysis on the McCracken-Abraham scheme and select an appropriate $\mathbf{Q_m}$ to adjust the coexistence densities. However, instead of following this approach, we propose a new pseudopotential force. Interestingly, the additional term in our new pseudopotential force can also be represented by $\mathbf{\Lambda Q_m}$. If we take the pseudopotential force as $\boldsymbol{F}_{\mathbf{new}} = -G\psi\tilde{\nabla}\psi$, which is the original pseudopotential force, then the additional term in our model can be expressed as

$$\boldsymbol{F}_{\mathbf{add}} = -2\gamma\tilde{\nabla}^2\psi\tilde{\nabla}\psi = 2\gamma\tilde{\nabla}^2\psi\frac{\boldsymbol{F}_{\mathbf{new}}}{G\psi}. \tag{71}$$

The corresponding $\mathbf{\Lambda Q_m}$ can be obtained by substituting Eq. (71) into Eq. (23):

$$\mathbf{Q}_{\mathbf{m}}^{\mathbf{our}} = 2\delta_t\gamma\tilde{\nabla}^2\psi\left(\mathbf{\Lambda}^{-1} - \tfrac{1}{2}\right)[0, Q_{\mathrm{m1}}, Q_{\mathrm{m2}}, Q_{\mathrm{m3}}, Q_{\mathrm{m4}}, Q_{\mathrm{m5}}, Q_{\mathrm{m6}}, Q_{\mathrm{m7}}, Q_{\mathrm{m8}}]^{\mathrm{T}}, \tag{72}$$

where $\mathbf{\Lambda}^{-1}$ is the inverse matrix of $\mathbf{\Lambda}$ and the components $Q_{\mathrm{m}i}$ are given by

$$\begin{aligned} Q_{\mathrm{m1}} &= \frac{6\bar{\boldsymbol{F}}_{\mathbf{pp}}\cdot\bar{\boldsymbol{u}}}{G\psi}, \quad Q_{\mathrm{m2}} = -\frac{6\bar{\boldsymbol{F}}_{\mathbf{pp}}\cdot\bar{\boldsymbol{u}}}{G\psi}, \quad Q_{\mathrm{m3}} = \frac{\bar{F}_{\mathrm{pp},x}}{G\psi}, \quad Q_{\mathrm{m4}} = -\frac{\bar{F}_{\mathrm{pp},x}}{G\psi}, \quad Q_{\mathrm{m5}} = \frac{\bar{F}_{\mathrm{pp},y}}{G\psi}, \\ Q_{\mathrm{m6}} &= -\frac{\bar{F}_{\mathrm{pp},y}}{G\psi}, \quad Q_{\mathrm{m7}} = \frac{2(\bar{F}_{\mathrm{pp},x}\bar{u}_x - \bar{F}_{\mathrm{pp},y}\bar{u}_y)}{G\psi}, \quad Q_{\mathrm{m8}} = \frac{(\bar{F}_{\mathrm{pp},x}\bar{u}_y + \bar{F}_{\mathrm{pp},y}\bar{u}_x)}{G\psi}. \end{aligned} \tag{73}$$

Equations (72) and (73) provide the corresponding additional term $\mathbf{Q_m}$ in our model. Although a third-order CE analysis was not conducted, the appropriate $\mathbf{Q_m}$ is still derived in this manner.

VI. MODEL VALIDATION

In this section, we thoroughly validate the applicability of our model under transient and moving conditions and analyze the accuracy of our pseudopotential model in simulating two-phase flows. It is well-established that the LBM exhibits second-order accuracy in simulating single-phase fluids [39]. However, the accuracy of the pseudopotential model in simulating two-phase flow has been less frequently reported. Among the few studies that do address this, some focus on simulating single-phase flow to evaluate the model's accuracy [22,45], while others compare coexistence densities [22,55,56] or surface tensions [57] of a stationary droplet for various sizes as accuracy indicators. The former primarily reflects the accuracy of the model in single-phase flow, while the latter evaluates the influence of surface tension on coexistence density. Clearly, neither approach fully captures the model's accuracy in simulating two-phase flows, particularly under transient and moving conditions.

To address this gap, we conducted simulations of two-phase Couette flow and two-phase Poiseuille flow for various values of k. These simulations not only validate the applicability of our model under transient and moving conditions,

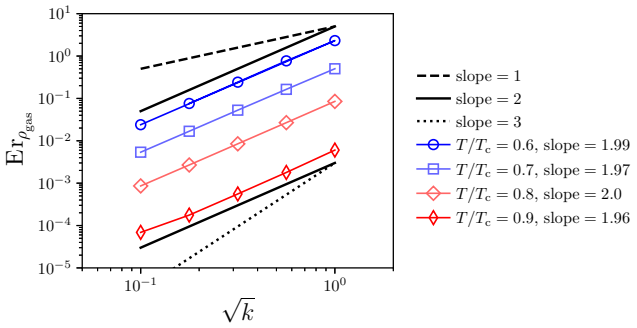

FIG. 10. Variation of $\mathrm{Er}_{\rho_{\mathrm{gas}}}$ with $\sqrt{k}$ for various temperatures.

but also demonstrate that our model achieves second-order accuracy in simulating two-phase flows. To the best of our knowledge, this is the first report on the accuracy of the pseudopotential model in simulating two-phase flows. In addition, please see Supplemental Material [58] for the model codes.

A. Accuracy of coexistence densities

The coexistence densities have been discussed in detail. This section focuses on the accuracy of our model in predicting the coexistence densities. The simulation settings are consistent with those in Sec. V B. As shown in Fig. 7, the difference between the LBM results and the mechanical stability for the gas phase is greater than that for the liquid phase. Therefore, we use the error in the gas density to quantify the error of our pseudopotential model. The error in the gas density $\mathrm{Er}_{\rho_{\mathrm{gas}}}$ is defined as

$$\mathrm{Er}_{\rho_{\mathrm{gas}}} = \left|\rho_{\mathrm{gas}}^{\mathrm{LBM}} - \rho_{\mathrm{gas}}^{\mathrm{Mech}}\right| / \rho_{\mathrm{gas}}^{\mathrm{Mech}}, \tag{74}$$

where $\rho_{\mathrm{gas}}^{\mathrm{LBM}}$ is the gas density calculated by LBM and $\rho_{\mathrm{gas}}^{\mathrm{Mech}}$ is the gas density given by the mechanical stability. The parameter ϵ is taken as 2.

Equation (67) demonstrates that the effect of k is equivalent to changing δ_x to $\sqrt{k}\delta_x$. Thus, we can analyze the variation of $\mathrm{Er}_{\rho_{\mathrm{gas}}}$ with $\sqrt{k}$ to assess the accuracy of our pseudopotential model. The corresponding results are shown in Fig. 10. The slope is obtained by fitting $\lg(\mathrm{Er}_u) = c_1 \lg(\sqrt{k}) + c_2$ to the data, where c_1 is the slope and c_2 is the intercept. It can be observed that the best-fit slope of the results is consistently around 2, indicating that our pseudopotential model exhibits second-order accuracy. Additionally, it can be seen that the error increases as the temperature decreases for a given k. This is because the interface thickness decreases as the temperature decreases, as shown in Fig. 8. The reduction in interface thickness leads to larger errors.

B. Two-phase Couette and Poiseuille Flow

The success of our model in eliminating interfacial velocity slip is validated by simulating two-phase Couette flow. In this section, the calculated domain length is taken as $50/\sqrt{k}$, with ϵ set to 2. The other simulation settings are consistent with those in Sec. IV C. Figure 11 compares the variations in velocity profiles and reduced shear stress with x for various temperatures, with $k = 1$. The density ratios given by the Maxwell construction for the temperatures $T = 0.948T_c$, $T = 0.901T_c$, and $T = 0.725T_c$ are 5.03, 10.04, and 100.34, respectively. Thus. these temperatures were chosen for the calculations. The results show that the velocity profiles agree well with the analytical solutions. For $T/T_c = 0.725$, there is no apparent difference between the calculated results and the analytical solutions. The shear stress oscillation in our model is of the same order of magnitude as that of the McCracken-Abraham scheme, with both being much smaller than those from other schemes.

We use Er_u to characterize the velocity error of our model. Er_u is defined as follows:

$$\mathrm{Er}_u = \frac{\sqrt{\sum_{i,j}\left[\hat{\tau}_u(i,j)\right]^2}}{N_x N_y}. \tag{75}$$

Figure 12 shows the variation of Er_u with $\sqrt{k}$ for various temperatures. The results demonstrate that the best-fit slopes are around 2, further indicating that our model exhibits second-order accuracy. It can be observed that the slopes are slightly

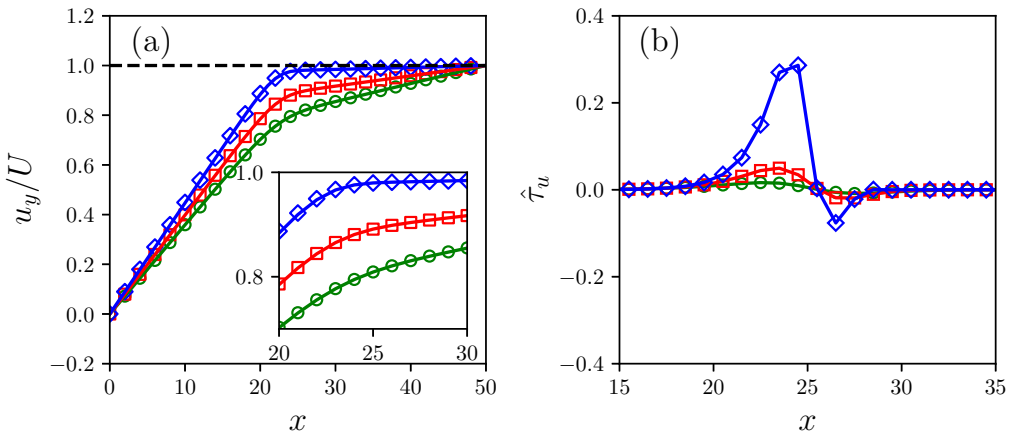

FIG. 11. (a) Velocity profiles of two-phase Couette flow for various temperatures. Points represent the analytical solutions and solid lines represent the calculated results. (b) Reduced shear stress for various temperatures. Connect points with lines for visual enhancement. The green line and rhombus points correspond to $T/T_c = 0.948$. The red line and square points correspond to $T/T_c = 0.901$. The blue line and circle points correspond to $T/T_c = 0.725$.

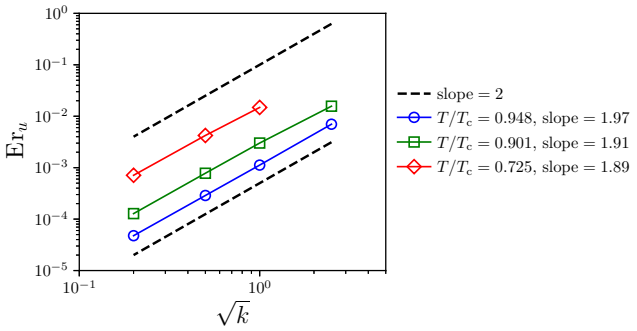

FIG. 12. Variation of Er_u with $\sqrt{k}$ for various temperatures.

less than 2 and that the bias increases as the temperature decreases. This is because the coexistence densities vary with k and this variation increases as the temperature decreases, as shown in Figs. 7 and 8. Figure 12 also shows that the error increases as the temperature decreases for a given k, consistent with the results in Fig. 10. This is because the interface thickness decreases with temperature, which leads to larger errors. By compariing Figs. 3 and 4, we find that increasing the interface thickness weakens the interface velocity slip. A similar phenomenon has also been discussed in the color gradient model [59]. Therefore, it is necessary to compare our model's behavior with other models under identical interface thicknesses. We take Li *et al.*'s MRT scheme and the Huang-Wu scheme as examples. The two-phase Couette flow was simulated for comparison. In the comparison, all physical property parameters and initialization methods were identical. The specific physical property values are $k = 0.25$, $\epsilon = 2$, $T = 0.7T_c$, $\tau = 0.8$; the velocity of the right wall U is 0.01; initialization is carried out according to Eq. (35) with $W = 5$; and the computational domain size is 200×3. Figure 13(a) compares the density profiles from different models. It shows that the density profiles of all three agree well with the analytical solutions and possess very similar interface thicknesses. Figure 13(b) shows the velocity profiles of the different models. Since k in this example is set to 0.25, the interface is thickened. Compared to Fig. 4, the interfacial velocity slip is suppressed. The degree of slip is close to that of the ST-EOS model in Fig. 4(f), but it remains clearly evident. However, our model exhibits no interface velocity slip. This fully demonstrates the advantages of our model.

Figure 13(a) also reveals that the gas density predicted by our model shows a greater deviation from the analytical solution than the other two force schemes. Specifically, our model yields a gas-phase density of 6.89×10^{-2}, compared to 6.37×10^{-2} for Li *et al.*'s force scheme and 6.37×10^{-2} for the Huang-Wu scheme. The analytical solution is 6.10×10^{-2}, indicating our model indeed exhibits a relatively large deviation. This discrepancy accounts for why, as depicted in Fig. 7, the predicted gas-phase density of our model at $T = 0.7T_c$ exhibits a significant deviation from mechanical stability with the negligible deviations observed in Li *et al.*'s MRT and Huang-Wu schemes (as illustrated in Fig. 1).We speculate that this discrepancy could be attributed to the relatively larger coefficient of the fifth-order term in our model compared to other models. This aspect merits detailed future investigation.

Additionally, we evaluated the stability of our model for this case in Fig. 13. By adjusting the dimensionless relaxation time τ, we determined the critical stability threshold. The results demonstrate that all three models converge successfully at $\tau = 0.5130(\nu = 1/230)$ but diverge at $\tau = 0.5125(\nu = 1/240)$, indicating comparable stability across the models. The newly added terms enhance the stability of McCracken-Abraham scheme to a level comparable with Li *et al.*'s and Huang-Wu schemes.

Two-phase Poiseuille flow is also simulated to further validate our model. The parameter k is set to 0.25 and τ is taken as 1.5. Other settings in this section remain the same as those in Sec. IV B. Figure 14 shows the velocity profiles for two-phase Poiseuille flow. The results demonstrate excellent agreement with the analytical solutions across all density ratios. Our model successfully eliminates interfacial velocity while adjusting the coexistence densities.

C. Young-Laplace equation

For a stationary droplet, the pressure inside the droplet is greater than the pressure outside due to the effect of surface tension. The pressure difference across the liquid-gas interface can be calculated using the Young-Laplace equation

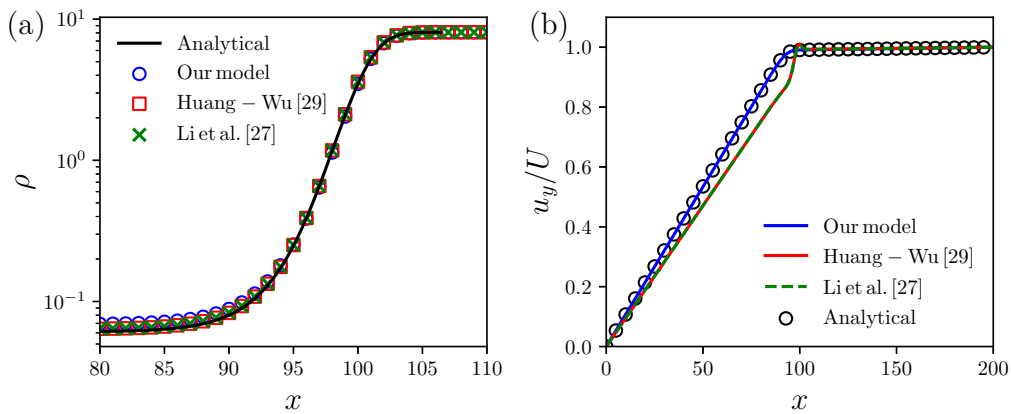

FIG. 13. (a) Comparison of density profiles of different models. (b) Comparison of two-phase Couette flow velocity profiles of different models.

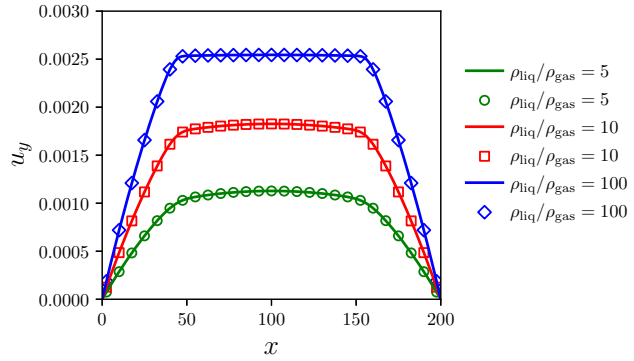

FIG. 14. Velocity profiles of two-phase Poiseuille flows for $\epsilon = 2$. Points represent the analytical solutions and the solid lines represent the calculated results. The results for $\rho_{liq}/\rho_{gas} = 100$ are scaled by a factor of 0.2.

$\Delta p = p_{liq} - p_{gas} = \sigma_{lg}/R$, where R represents the droplet radius and σ_{lg} is the surface tension. The surface tension can be derived from pressure tensor $\mathbf{P}$ using the following formula:

$$\sigma_{lg} = \int_{-\infty}^{+\infty} (P_{xx} - P_{yy}) \mathrm{d}x = (2\gamma - \kappa_{new}) \int_{\rho_{gas}}^{\rho_{liq}} \left[\left(\frac{\mathrm{d}\psi}{\mathrm{d}\rho} \right)^2 \frac{\mathrm{d}\rho}{\mathrm{d}x} \right] \mathrm{d}\rho. \quad (76)$$

In this section, the calculated domain size is $L_x \times L_y = 200 \times 200$. The parameters k is set to 1 and τ is set to 1.5. The density field of the stationary droplet is initialized as follows:

$$\rho(\boldsymbol{x}) = \frac{\rho_{liq} + \rho_{gas}}{2} - \frac{\rho_{liq} - \rho_{gas}}{2} \tanh \frac{2(|\boldsymbol{x} - \boldsymbol{x}_c| - R_{init})}{W_{init}}, \quad (77)$$

where $\boldsymbol{x}_c = [L_x/2, L_y/2]$ represents the center position of the domain and R_{init} is the initial radius of the droplet. In this work, the contour line for $\rho = (\rho_{liq} + \rho_{gas})/2$ is fitted using the circle formula and the best-fit radius is considered the droplet radius R. Figure 15 shows the variations of Δp with $1/R$. The surface tensor σ_{lg} calculated by Eq. (76) has been labeled in Fig. 15. It can be seen that Δp and $1/R$ satisfy a good linear relationship and the calculated results are in good agreement with the analytical solutions, further validating our model.

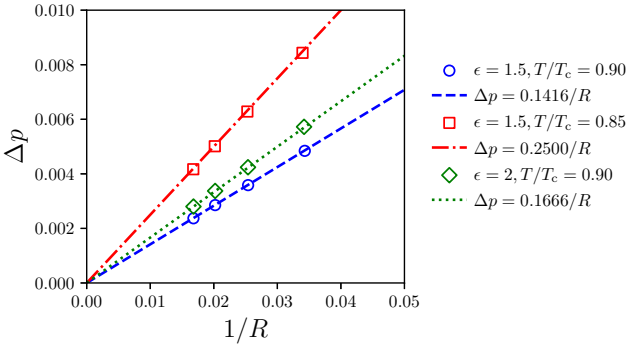

FIG. 15. Variations of Δp with $1/R$. Points represent the results from LBM and the lines represent the analytical solutions. The same color corresponds to the same parameter settings.

D. Transient flows

The above validations focus on steady-state cases; however, the applicability of our model under transient conditions has yet to be validated. Since few analytical solutions exist for transient two-phase flow, we compare the transient results of our model with those obtained using the VOF method [6]. For simulating transient two-phase Couette flow, the right boundary is initially set as a no-slip wall. Once the convergence condition from Eq. (31) is satisfied, a constant velocity boundary condition is applied to the right boundary and timekeeping begins. A similar procedure is followed for two-phase Poiseuille flow. In this section, we set $\tau = 1$, $k = 1$, $\epsilon = 2$, and $T = 0.8T_c$. The coexistence densities calculated by our model are $\rho_{gas} = 0.247$ and $\rho_{liq} = 7.211$, which are then used as the gas and liquid densities for the calculations using the VOF method.

Since the VOF method is not the focus of this work, details of this method can be found in Refs. [5,6]. VOF simulations are performed using ANSYS Fluent software with 10 iterations per time step and the velocity residuals were reduced to 10^{-6} per time step. Other parameters are kept consistent with the LB simulations. In contrast to LBM, the VOF method is a sharp-interface method. Therefore, some bias in the density profile between the two methods is inevitable, as shown in Figs. 16(a) and 16(b). This bias results in discrepancies in the velocity profiles.

Figure 16(c) shows a comparison of the velocity profiles for Couette flow calculated by LBM and VOF. The results indicate that the LBM results agree well with those from the VOF method. Initially, there is no noticeable bias between the two methods. However, as the velocity diffuses toward the interface, some bias appears near the interface, which can be attributed to the density profile bias. The comparison of Poiseuille flow velocity profiles is shown in Fig. 16(d). Both methods exhibit good agreement, with the velocity bias in the liquid region being smaller than in the gas region. Since Poiseuille flow involves two interfaces, whereas Couette flow has only one, the effect of the density profile bias is more pronounced in Poiseuille flow than in Couette flow. Overall, the results from both our model and the VOF method show good agreement, with no nonphysical phenomena such as interfacial velocity slip in our model. These results fully validate the applicability of our model under transient and moving conditions.

E. Droplet splashing

Droplet splashing on thin liquid films is widely used to validate pseudopotential models [27,45]. For this simulation, a 1000×250 computational domain is employed. Nonslip boundaries at the top and bottom are implemented using the Zou-He scheme, while periodic boundaries are applied to the left and right sides. The parameters are set to $k = 0.25$, $\epsilon = 2$, with an operating temperature of $0.7T_c$. At this temperature, the liquid density is 8.0807 and the gas density is 0.0609. Initially, a droplet of diameter $D = 100$ is positioned at the center with initial velocity $\boldsymbol{u} = (0, -0.1)$. A liquid film of thickness 25 covers the lower wall. We define $t_s = (t - t_0)|\boldsymbol{u}|/D$, where t_0 is the contact moment between the droplet and liquid film. For this simulation, $t_0 = 500$. The kinematic viscosity

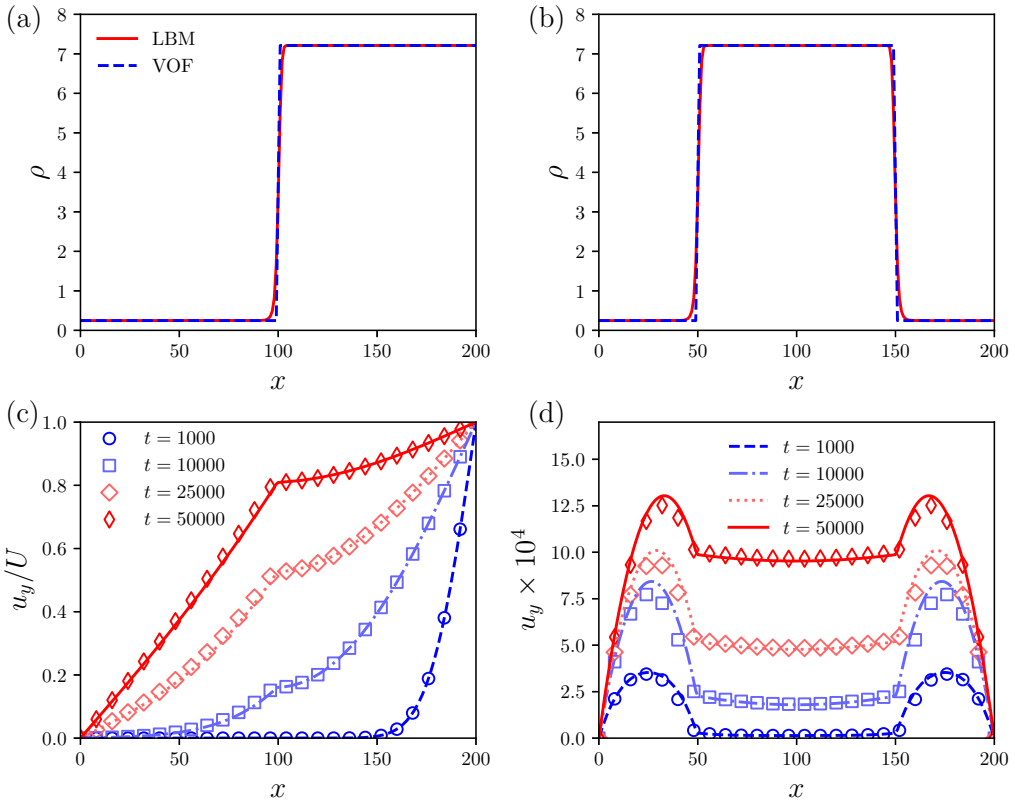

FIG. 16. (a), (b) Density profiles of two-phase (a) Couette and (b) Poiseuille flows. (c), (d) Velocity profiles of two-phase (c) Couette and (d) Poiseuille flows for various times. Points represent the results of LBM. Lines represent the results of VOF.

is adjusted to achieve different Reynolds numbers, defined as $\mathrm{Re} = |\boldsymbol{u}|D/\nu$.

In droplet splashing simulations, the diffusion radius r consistently follows a power-law relationship with time: $r/D = C\sqrt{t_s}$. The constant C is typically approximately 1.3, with Li *et al.* reporting 1.3 and Wu *et al.* [45] reporting 1.27. Here, r is defined as the distance from the droplet center to the position of maximum velocity [60]. Figure 17 presents our model's simulation results for various Re. It clearly demonstrates that r/D and t_s maintain an excellent power-law relationship, showing good agreement with the results reported by Wu *et al.* [45]. This consistency further validates our model.

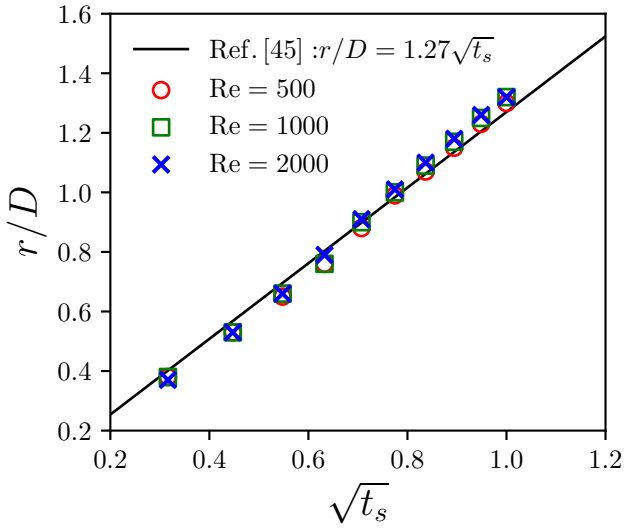

FIG. 17. Variation of r/D with $\sqrt{t_s}$ for various Re.

F. Liquid film evaporation under shear flow

The pseudopotential model can effectively predict interphase mass transfer. The Schrage equation derived from kinetic theory can predict the interphase mass transfer well [20,61]:

$$\dot{m} = \frac{2\overline{\sigma}}{2-\overline{\sigma}}\left(\frac{M_\mathrm{f}}{2\pi\overline{R}}\right)^{1/2}\left[\frac{p_{\mathrm{v,equ}}(T_\mathrm{lv})}{T_\mathrm{lv}^{1/2}} - \frac{p_\mathrm{v}}{T_\mathrm{v}^{1/2}}\right], \tag{78}$$

where $\dot{m}$ is the interfacial mass flux, $\overline{\sigma}$ is the mass accommodation coefficient, M_f is the molar mass of the fluid, $\overline{R}$ is the universal gas constant, T_lv is the interface temperature, p_v and T_v are the vapor pressure and temperature far from the interface, and $p_{\mathrm{v,equ}}(T_\mathrm{lv})$ denotes the equilibrium pressure at T_lv. Under constant temperature conditions, Eq. (78) can be simplified to

$$\dot{m} = C(p_{\mathrm{v,equ}} - p_\mathrm{v}) = C\Delta p, \tag{79}$$

where C is constant. This indicates that liquid films evaporate continuously when the distant pressure is below the saturated vapor pressure, and condense continuously otherwise. This section simulates such behavior using physical parameters consistent with Sec. VI E and $\tau = 1$. The computational domain is 200×3 with a no-slip wall at the left boundary. The right boundary employs the Zou-He scheme with constant pressure p_v and constant $u_y = 0.01$, while u_x is computed

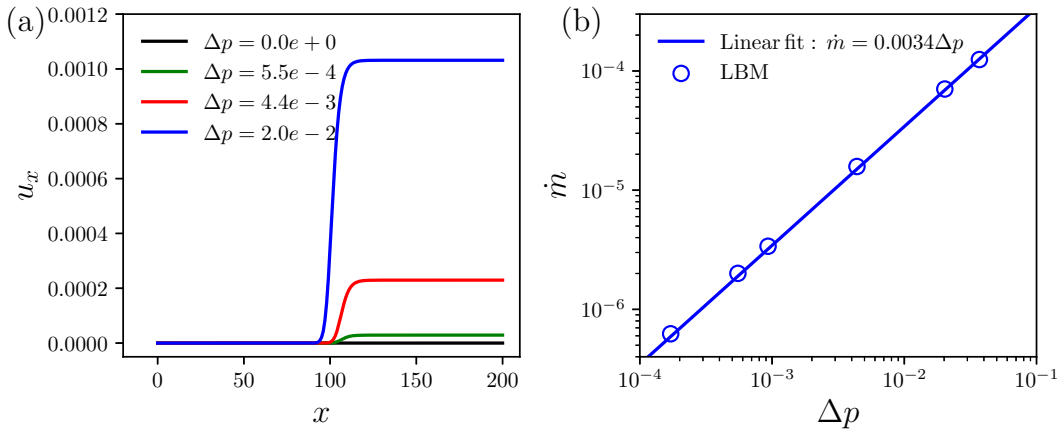

FIG. 18. (a) Variation of u_x with x for various Δp. (b) Variation of $\dot{m}$ with Δp.

via LBM. By varying p_v, different Δp values are achieved. Density initialization follows Eq. (79).

Figure 18(a) displays u_x profiles for various Δp. There is no mass transfer while $\Delta p = 0$ and $u_x = 0$. u_x in the gas phase increases with Δp. Figure 18(b) shows $\dot{m}$ versus Δp, revealing a strong linear relationship over a wide range. This corresponds to $C = 0.0034$ in Eq. (79). Notably, in this section, interphase mass transfer occurs under shear conditions, demonstrating our model's capability for predicting interphase mass transfer.

VII. CONCLUSION

Over the past 30 years, various force schemes have been proposed to achieve thermodynamic consistency by adjusting coexistence densities. However, the performance of these force schemes under transient and moving conditions has not been thoroughly validated. To address this gap, we first evaluate the applicability of existing force schemes under transient and moving conditions. We find that most schemes [11,25–27,29,31] suffer from interfacial velocity slip. This is manifested as a discontinuity in the velocity near the liquid-gas interface, marked by a sharp rise or fall. The underlying cause of this velocity slip is the shear stress oscillation. Our CE analysis reveals that other schemes introduce error terms related to force and velocity in the macroscopic equations, leading to the shear stress oscillation and the interfacial velocity slip.

While the schemes proposed by Guo *et al.* [23] and McCracken-Abraham [24] do not result in interfacial velocity slip, they fail to adjust coexistence densities. To address this limitation and achieve thermodynamic consistency, we propose a new pseudopotential model. This model introduces a novel pseudopotential force, which adds an additional term, $-2\gamma\tilde{\nabla}^2\psi\tilde{\nabla}\psi$, to the original force. Thermodynamic consistency is achieved by tuning the parameter γ. Moreover, we provide a comprehensive discussion on the underlying mechanisms of adjusting the interface thickness through the new pressure term $p_{\mathrm{EOS}}^{\mathrm{new}} = kp_{\mathrm{EOS}}$. By performing unit conversion, we demonstrate that the parameter k can adjust the interface thickness in lattice units, but it does not affect the interface thickness in physical units. The effect of k is equivalent to scaling the spatial step in physical units by a factor of $\sqrt{k}$.

The applicability of our model under transient and moving conditions is thoroughly validated through various test cases. We simulate two-phase Couette and Poiseuille flows, with the results demonstrating excellent agreement with analytical solutions. Our model successfully adjusts the coexistence densities while eliminating interfacial velocity slip. Furthermore, numerical tests confirm that our model exhibits second-order accuracy, which is the first report on the accuracy of the pseudopotential model in simulating two-phase flows. A stationary droplet simulation further validates the surface tensor, with results showing excellent alignment with analytical solutions. Additionally, we compare the transient results of our model with those from the VOF method. The transient velocity profiles from both methods exhibit close alignment, further validating the our model under transient conditions. Finally, droplet splashing and liquid film evaporation under shear flow are also simulated to demonstrate our model's capability for simulating two-dimensional flow and interfacial mass transfer.

ACKNOWLEDGMENTS

This work was funded by the China National Nuclear Corporation's R&D Platform Stabilization Support Research Project (Grant No. WDZC-2024-SKL106). We thank Zhaoqi Zheng for helpful discussions on the manuscript.

DATA AVAILABILITY

The data that support the findings of this article are openly available [58].

[1] Y. Sun, A. Huang, J. Lu, and Y. Jiang, Flow boiling characteristics of ethanol in a microchannel with low mass flux, Int. J. Heat Mass Transf. **219**, 124845 (2024).

[2] T. Ren, Z. Zhu, M. Yan, J. Shi, and C. Yan, Experimental study on bubble nucleation and departure for subcooled flow boiling in a narrow rectangular channel, Int. J. Heat Mass Transf. **144**, 118670 (2019).

[3] J. Gregorc, Numerical prediction of maldistribution in a series of T-junctions, Chem. Eng. Sci. **239**, 116647 (2021).

[4] J. Chen, S. Ahmad, W. Deng, J. Cai, and J. Zhao, Micro/nanoscale surface on enhancing the microchannel flow boiling performance: A lattice Boltzmann simulation, Appl. Therm. Eng. **205**, 118036 (2022).

[5] L. Wei, L.-M. Pan, Y.-M. Zhao, Q.-Y. Ren, and W.-Z. Zhang, Numerical study of adiabatic two-phase flow patterns in vertical rectangular narrow channels, Appl. Therm. Eng. **110**, 1101 (2017).

[6] C. Hirt and B. Nichols, Volume of fluid (VOF) method for the dynamics of free boundaries, J. Comput. Phys. **39**, 201 (1981).

[7] S. Osher and J. A. Sethian, Fronts propagating with curvature-dependent speed: Algorithms based on Hamilton-Jacobi formulations, J. Comput. Phys. **79**, 12 (1988).

[8] J. Song, N. Gui, T. Lu, X. Yang, and S. Jiang, Refining LBM accuracy and efficiency for neutron diffusion: Integrated strategies for model configuration and boundary treatment, Ann. Nucl. Energy **223**, 111638 (2025).

[9] Q. Li, Y. Yu, and R. Z. Huang, Achieving thermodynamic consistency in a class of free-energy multiphase lattice Boltzmann models, Phys. Rev. E **103**, 013304 (2021).

[10] A. K. Gunstensen, D. H. Rothman, S. Zaleski, and G. Zanetti, Lattice Boltzmann model of immiscible fluids, Phys. Rev. A **43**, 4320 (1991).

[11] X. Shan and H. Chen, Lattice Boltzmann model for simulating flows with multiple phases and components, Phys. Rev. E **47**, 1815 (1993).

[12] X. Shan and H. Chen, Simulation of nonideal gases and liquid-gas phase transitions by the lattice Boltzmann equation, Phys. Rev. E **49**, 2941 (1994).

[13] X. He, S. Chen, and R. Zhang, A lattice Boltzmann scheme for incompressible multiphase flow and its application in simulation of Rayleigh–Taylor instability, J. Comput. Phys. **152**, 642 (1999).

[14] T. Lee and C.-L. Lin, A stable discretization of the lattice Boltzmann equation for simulation of incompressible two-phase flows at high density ratio, J. Comput. Phys. **206**, 16 (2005).

[15] Q. Li, K. Luo, Q. Kang, Y. He, Q. Chen, and Q. Liu, Lattice Boltzmann methods for multiphase flow and phase-change heat transfer, Prog. Energy Combust. Sci. **52**, 62 (2016).

[16] X. He and G. D. Doolen, Thermodynamic foundations of kinetic theory and lattice Boltzmann models for multiphase flows, J. Stat. Phys. **107**, 309 (2002).

[17] P. Yuan and L. Schaefer, Equations of state in a lattice Boltzmann model, Phys. Fluids **18**, 042101 (2006).

[18] Z. Zheng and Y. Huang, Implementation of fundamental equations of state in a lattice Boltzmann model, Phys. Fluids **37**, 023352 (2025).

[19] S. Gong, F. Hong, Q. Guo, L. Zhang, and P. Cheng, Mesoscopic approach for nanoscale liquid-vapor interfacial statics and dynamics, Int. J. Heat Mass Transf. **194**, 123104 (2022).

[20] S. Gong, Z. Hu, and P. Cheng, A mesoscopic approach for nanoscale evaporation heat transfer characteristics, Int. J. Heat Mass Transf. **231**, 125856 (2024).

[21] J. Hou, M. Liu, and S. Huang, Lattice boltzmann simulations of Rayleigh–Bénard convection with compressibility-induced non-Oberbeck–Boussinesq effects, J. Fluid Mech. **1009**, A49 (2025).

[22] H. Huang, M. Krafczyk, and X. Lu, Forcing term in single-phase and Shan-Chen-type multiphase lattice Boltzmann models, Phys. Rev. E **84**, 046710 (2011).

[23] Z. Guo, C. Zheng, and B. Shi, Discrete lattice effects on the forcing term in the lattice Boltzmann method, Phys. Rev. E **65**, 046308 (2002).

[24] M. E. McCracken and J. Abraham, Multiple-relaxation-time lattice-Boltzmann model for multiphase flow, Phys. Rev. E **71**, 036701 (2005).

[25] A. Kupershtokh, D. Medvedev, and D. Karpov, On equations of state in a lattice Boltzmann method, Comput. Math. Appl. **58**, 965 (2009).

[26] Q. Li, K. H. Luo, and X. J. Li, Forcing scheme in pseudopotential lattice Boltzmann model for multiphase flows, Phys. Rev. E **86**, 016709 (2012).

[27] Q. Li, K. H. Luo, and X. J. Li, Lattice Boltzmann modeling of multiphase flows at large density ratio with an improved pseudopotential model, Phys. Rev. E **87**, 053301 (2013).

[28] D. Lycett-Brown and K. H. Luo, Improved forcing scheme in pseudopotential lattice Boltzmann methods for multiphase flow at arbitrarily high density ratios, Phys. Rev. E **91**, 023305 (2015).

[29] R. Huang and H. Wu, Third-order analysis of pseudopotential lattice Boltzmann model for multiphase flow, J. Comput. Phys. **327**, 121 (2016).

[30] L. Zheng, Q. Zhai, and S. Zheng, Analysis of force treatment in the pseudopotential lattice Boltzmann equation method, Phys. Rev. E **95**, 043301 (2017).

[31] R. Huang, H. Wu, and N. A. Adams, Lattice Boltzmann model with self-tuning equation of state for multiphase flows, Phys. Rev. E **99**, 023303 (2019).

[32] R. Huang, H. Wu, and N. A. Adams, Lattice Boltzmann model with adjustable equation of state for coupled thermo-hydrodynamic flows, J. Comput. Phys. **392**, 227 (2019).

[33] R. Huang, H. Wu, and N. A. Adams, Mesoscopic lattice Boltzmann modeling of the liquid-vapor phase transition, Phys. Rev. Lett. **126**, 244501 (2021).

[34] Q. Li, Y. Xing, and R. Huang, Equations of state in multiphase lattice Boltzmann method revisited, Phys. Rev. E **107**, 015301 (2023).

[35] A. J. Wagner and C. M. Pooley, Interface width and bulk stability: Requirements for the simulation of deeply quenched liquid-gas systems, Phys. Rev. E **76**, 045702(R) (2007).

[36] A. Hu, L. Li, S. Chen, Q. Liao, and J. Zeng, On equations of state in pseudo-potential multiphase lattice Boltzmann model with large density ratio, Int. J. Heat Mass Transf. **67**, 159 (2013).

[37] H. Deng, K. Jiao, Y. Hou, J. W. Park, and Q. Du, A lattice Boltzmann model for multi-component two-phase gas-liquid flow with realistic fluid properties, Int. J. Heat Mass Transf. **128**, 536 (2019).

[38] Y. Wu, N. Gui, X. Yang, J. Tu, and S. Jiang, Fourth-order analysis of force terms in multiphase pseudopotential lattice Boltzmann model, Comput. Math. Appl. **76**, 1699 (2018).

[39] T. Krüger, H. Kusumaatmaja, A. Kuzmin, O. Shardt, G. Silva, and E. M. Viggen, *The Lattice Boltzmann Method—Principles and Practice* (Spinger, Berlin, 2016).

[40] Y. H. Qian, D. D'Humières, and P. Lallemand, Lattice BGK models for Navier-Stokes equation, Europhys. Lett. **17**, 479 (1992).

[41] P. Lallemand and L.-S. Luo, Theory of the lattice Boltzmann method: Dispersion, dissipation, isotropy, Galilean invariance, and stability, Phys. Rev. E **61**, 6546 (2000).

[42] R. Huang, Q. Li, and N. A. Adams, Surface thermodynamics and wetting condition in the multiphase lattice Boltzmann model with self-tuning equation of state, J. Fluid Mech. **940**, A46 (2022).

[43] A. J. Wagner, Thermodynamic consistency of liquid-gas lattice Boltzmann simulations, Phys. Rev. E **74**, 056703 (2006).

[44] D. Lycett-Brown and K. H. Luo, Cascaded lattice Boltzmann method with improved forcing scheme for large-density-ratio multiphase flow at high Reynolds and Weber numbers, Phys. Rev. E **94**, 053313 (2016).

[45] Y. Wu, N. Gui, X. Yang, J. Tu, and S. Jiang, A decoupled and stabilized lattice Boltzmann method for multiphase flow with large density ratio at high Reynolds and Weber numbers, J. Comput. Phys. **426**, 109933 (2021).

[46] Q. Zou and X. He, On pressure and velocity boundary conditions for the lattice Boltzmann BGK model, Phys. Fluids **9**, 1591 (1997).

[47] H. Huang and X.-y. Lu, Relative permeabilities and coupling effects in steady-state gas-liquid flow in porous media: A lattice Boltzmann study, Phys. Fluids **21**, 092104 (2009).

[48] H. Huang, M. Sukop, and X. Lu, *Shan and Chen-Type Multi-Component Multiphase Models* (John Wiley & Sons, New York, NY, 2015), Ch. 3, pp. 71–93.

[49] R. Huang, H. Wu, and N. A. Adams, Density gradient calculation in a class of multiphase lattice Boltzmann models, Phys. Rev. E **100**, 043306 (2019).

[50] C. Zhang, Z. Guo, and H. Liang, High-order lattice-Boltzmann model for the Cahn-Hilliard equation, Phys. Rev. E **99**, 043310 (2019).

[51] F. Dubois and P. Lallemand, Towards higher order lattice Boltzmann schemes, J. Stat. Mech.: Theory Exp. (2009) P06006.

[52] G. Silva and V. Semiao, Truncation errors and the rotational invariance of three-dimensional lattice models in the lattice Boltzmann method, J. Comput. Phys. **269**, 259 (2014).

[53] M. Geier, A. Greiner, and J. G. Korvink, Cascaded digital lattice Boltzmann automata for high Reynolds number flow, Phys. Rev. E **73**, 066705 (2006).

[54] K. N. Premnath and S. Banerjee, Incorporating forcing terms in cascaded lattice Boltzmann approach by method of central moments, Phys. Rev. E **80**, 036702 (2009).

[55] A. Xu, T. Zhao, L. An, and L. Shi, A three-dimensional pseudopotential-based lattice Boltzmann model for multiphase flows with large density ratio and variable surface tension, Int. J. Heat Fluid Flow **56**, 261 (2015).

[56] L. Fei, J. Du, K. H. Luo, S. Succi, M. Lauricella, A. Montessori, and Q. Wang, Modeling realistic multiphase flows using a non-orthogonal multiple-relaxation-time lattice Boltzmann method, Phys. Fluids **31**, 042105 (2019).

[57] C. Peng, L. F. Ayala, and O. M. Ayala, A thermodynamically consistent pseudo-potential lattice Boltzmann model for multicomponent, multiphase, partially miscible mixtures, J. Comput. Phys. **429**, 110018 (2021).

[58] See Supplemental Material at http://link.aps.org/supplemental/10.1103/kpjp-fynh for the model codes. Most of the data in the paper can be calculated from the codes. Other data are available from the authors upon reasonable request.

[59] Y. Ba, H. Liu, Q. Li, Q. Kang, and J. Sun, Multiple-relaxation-time color-gradient lattice Boltzmann model for simulating two-phase flows with high density ratio, Phys. Rev. E **94**, 023310 (2016).

[60] C. Josserand and S. Zaleski, Droplet splashing on a thin liquid film, Phys. Fluids **15**, 1650 (2003).

[61] R. W. Schrage, *A Theoretical Study of Interphase Mass Transfer* (Columbia University Press, New York, NY, 1953).